Icarus 290 (2017) 14–45

Contents lists available at ScienceDirect

Icarus

journal homepage: www.elsevier.com/locate/icarus

Noncircular features in Saturn's rings IV: Absolute radius scale and Saturn's pole direction

Richard G. French[a,*], Colleen A. McGhee-French[a], Katherine Lonergan[b], Talia Sepersky[c], Robert A. Jacobson[d], Philip D. Nicholson[e], Mathew M. Hedman[f], Essam A. Marouf[g], Joshua E. Colwell[h]

[a] Department of Astronomy, Wellesley College, Wellesley, MA 02481, USA
[b] formerly Department of Astronomy, Wellesley College, Wellesley MA 02481, USA
[c] Museum of Science, Boston, MA 02114, USA
[d] Jet Propulsion Laboratory, California Institute of Technology, Pasadena, CA 91109, USA
[e] Department of Astronomy, Cornell University, Ithaca NY 14853, USA
[f] Department of Physics, University of Idaho, Moscow, ID 83844, USA
[g] Department of Electrical Engineering, San Jose State University, San Jose CA 95192, USA
[h] Department of Physics, University of Central Florida, Orlando FL 32816, USA

ARTICLE INFO

Article history:
Received 30 October 2016
Accepted 14 February 2017
Available online 20 February 2017

Keywords:
Occultations
Planets: Rings

ABSTRACT

We present a comprehensive solution for the geometry of Saturn's ring system, based on orbital fits to an extensive set of occultation observations of 122 individual ring edges and gaps. We begin with a restricted set of very high quality *Cassini* VIMS, UVIS, and RSS measurements for quasi-circular features in the C and B rings and the Cassini Division, and then successively add suitably weighted additional *Cassini* and historical occultation measurements (from *Voyager, HST* and the widely-observed 28 Sgr occultation of 3 Jul 1989) for additional non-circular features, to derive an absolute radius scale applicable across the entire classical ring system. As part of our adopted solution, we determine first-order corrections to the spacecraft trajectories used to determine the geometry of individual occultation chords. We adopt a simple linear model for Saturn's precession, and our favored solution yields a precession rate on the sky $\dot{\hat{n}}_P = 0.207 \pm 0.006''\mathrm{yr}^{-1}$, equivalent to an angular rate of polar motion $\Omega_P = 0.451 \pm 0.014''\mathrm{yr}^{-1}$. The 3% *formal* uncertainty in the fitted precession rate is approaching the point where it can provide a useful constraint on models of Saturn's interior, although realistic errors are likely to be larger, given the linear approximation of the precession model and possible unmodeled systematic errors in the spacecraft ephemerides. Our results are largely consistent with independent estimates of the precession rate based on historical RPX times (Nicholson et al., 1999 AAS/Division for Planetary Sciences Meeting Abstracts #31 31, 44.01) and from theoretical expectations that account for Titan's 700-yr precession period (Vienne and Duriez 1992, Astronomy and Astrophysics 257, 331–352). The fitted precession rate based on *Cassini* data only is somewhat lower, which may be an indication of unmodeled shorter term contributions to Saturn's polar motion from other satellites, or perhaps the result of inconsistencies in the assumed direction of Saturn's pole in the reconstructed *Cassini* spacecraft ephemerides. Overall, the agreement of our results with the widely-used French et al. (1993, Icarus 103, 163–214) radius scale is excellent, with very small ($\lesssim$ 0.1 km) *systematic* differences, although differences in a few individual feature radii are as large as 6 km. Our new solution incorporates many more features across the ring system, and the fitted orbital elements correct for the several-km biases in the radii of many ring features in the French et al. (1993) catalog that were unresolved because of the large projected diameter of the occulted star in the 28 Sgr event. The formal errors in the fitted radii are generally quite small – on the order of tens of meters. Systematic errors stemming from uncertainty in the precession rate of Saturn's pole and its effect on the accuracy of the reconstructed *Cassini* trajectories are somewhat larger, but the absolute radius scale is relatively insensitive to 5-σ changes in the pole direction or precession rate, and we estimate the combined magnitude of these systematic errors and pole uncertainties to be of order 250 m. This estimate

* Corresponding author.
E-mail addresses: rfrench@wellesley.edu, rfrench@wellesley.edu1 (R.G. French).

http://dx.doi.org/10.1016/j.icarus.2017.02.007

is likely to be improved once a new set of reconstructed *Cassini* trajectories has been developed, based on a self-consistent model for Saturn's pole. We demonstrate the utility of the new radius scale and the associated trajectory corrections in the analysis of short-wavelength density waves in the C ring. In online supplementary material, we provide in machine-readable form the more than 15,000 individual ring measurements used in this study, as well as details of the ring orbit fits underlying this work.

1. Introduction

Saturn's rings exhibit astonishing variety in form, structure, and underlying dynamics, providing a virtual laboratory for investigating the interactions of innumerable ring particles with the gravitational fields of Saturn, its retinue of small and large satellites, and each other. The radial structure of the classical rings was first revealed in detail from images and occultation measurements during the *Voyager 1* and *2* encounters in the early 1980s (Smith et al., 1981; 1982). Subsequent Earth-based occultations of 28 Sgr (French et al. 1993, henceforth F93, and Hubbard et al. 1993) contributed to the determination of an accurate absolute radius scale for the rings and the first measurement of the forced precession of Saturn's pole due to solar torques, with further refinements provided by two Earth-based stellar occultations observed using the *Hubble Space Telescope* (*HST*) (Elliot et al., 1993; Bosh et al., 2002).

A new era of investigation of Saturn's rings began in 2004, when the *Cassini* spacecraft began its orbital reconnaissance of the Saturn system that continues today. Using a suite of instruments and taking advantage of the widely varying viewing geometry provided by the *Cassini* orbital tour, ongoing studies have greatly expanded our understanding of the structure and dynamics of the rings (see Colwell et al. 2009 for an extensive review, and references cited therein). As part of this effort, we have combined the observations of literally hundreds of *Cassini* stellar and radio occultation experiments in a series of papers that investigate the structure of the non-circular features in Saturn's classical rings in unprecedented detail. In Nicholson et al. (2014a) (henceforth Paper 1), we determined the shape of the outer edge of Saturn's B ring using a combination of all available radio and stellar occultation data spanning the period 1980–2010, and identified both free and forced normal mode distortions of the ring edge. Next, in Nicholson et al. (2014b) (henceforth Paper 2), we examined all of the noncircular features in the C ring, identifying a host of systematic radial perturbations as small as 200 m on the edges of ringlets and gaps. In French et al. (2016b) (henceforth Paper 3), we explored the complex kinematical behavior of a host of noncircular ringlets and gap edges in the Cassini Division.

This paper is the fourth in our series of studies of sharp-edged ringlets and gaps in Saturn's rings. Here, we combine over 15,000 measurements of individual ring features from historical (pre-*Cassini*) and *Cassini* occultations to determine a highly accurate radius scale, from the inner edge of the C ring to the outer edge of the A ring, based on orbital fits to 116 features (both circular and non-circular) in the ring system. A crucial step in our solution is to solve for low-order corrections to the nominal *Cassini* spacecraft ephemerides for any given occultation, making it possible to relate the time of observation to the corresponding absolute radius probed in the equatorial plane with an uncertainty of order 250 m for all of the occultations in our data set. The resulting accurate absolute reference system undergirds quantitative studies of a host of weak dynamical effects that result in very small noncircularity or inclination in ring edges, as we have shown in Papers 1, 2 and 3. Our study has revealed the importance of correcting for systematic radial perturbations of the sharp edges of ringlets and gaps, and of broader features such as density and bending waves, driven by the $m = 1$ Titan 1:0 inner Lindblad resonance (ILR) in the C ring and 2:1 Mimas ILR in the Cassini Division, when aligning observations with the derived radius scale. It is also an essential component for detailed investigations of density and bending waves driven by satellites or Saturn itself (Hedman and Nicholson, 2013; 2014; French et al., 2016a) and for the determination of the direction and precession rate of Saturn's pole, providing an independent estimate of Saturn's moment of inertia. As a final example of the utility of our results, the catalog of sharp-edged features provides a reference system that enables accurate navigation of tens of thousands of spacecraft images of the rings in NASA's Planetary Data System (Robert French, personal communication).

Our presentation is organized as follows. We begin with a description of the occultation observations used in this study, reviewing the historical (pre-*Cassini*) data in Section 2 and presenting the *Cassini* observations in Section 3. Next, we describe the framework within which we establish the occultation geometry (Section 4), and then describe the least-squares fitting procedure used to determine the orbital elements of our atlas of ring features (Section 5). Our determination of the absolute ring radius scale and Saturn pole direction is given in Section 6, where we compare our results to the widely-used F93 radius scale, and we summarize our conclusions in Section 7. In the Appendix, we present sample calculations using our derived *Cassini* trajectory corrections and briefly describe the auxiliary material and machine-readable tables provided in the online supplementary material (henceforth SM).

2. Historical occultation observations

The fundamental observations used to establish the geometry of Saturn's ring system and pole are a host of measurements of individual sharp-edged ringlets and gap edges in occultation light curves. As described in detail in French et al. (2010, Section 3 and Eq. (6); henceforth F10), we begin by normalizing each occultation in intensity, and then fit a logistic model function to the normalized signal profile for each individual ring feature. Although the *Cassini* observations greatly outnumber the earlier occultations, these historical events extend the time baseline of the full set of observations to a span of over three decades (1980–2013), thereby contributing to the accuracy of the determination of long-term secular trends such as the precession of Saturn's pole and the apsidal and nodal precession of individual ring features. Here, we briefly describe these earlier data sets and identify references that contain detailed documentation of the observations.

2.1. Voyager *occultations*

The *Voyager* flybys of Saturn provided two separate high-resolution occultation scans of the ring system. The *Voyager 1* RSS egress occultation was observed on 1980 November 13 (Tyler et al., 1983). For this study, we make use of the diffraction-corrected observations obtained by Fresnel inversion (Marouf et al., 1986), yielding sub-km resolution profiles of all but the most opaque parts of the B ring, where the slant-path optical depth was very high owing to the very low ring opening angle ($B \simeq 6°$) at the time

of the observations.[1] As discussed below in the context of *Cassini* RSS occultation observations, we take account of small systematic biases in the measured radius of some ring features in the *Voyager 1* data set resulting from the finite resolution of the diffraction reconstruction filter. The complete set of measured *Voyager 1* RSS ring feature times used in our study is included in the online SM.

During the *Voyager 2* flyby, the egress stellar occultation of δ Sco was observed with the PPS (Lane et al. 1982; Esposito et al. 1983; 1987) and the UVS (Sandel et al., 1982; Holberg et al., 1982) instruments. For this study, we make use of the higher time resolution PPS data only; our fitted PPS ring feature times as described in F10 are also included in the SM.

Both *Voyager* data sets were previously analyzed by Nicholson et al. (1990) for the same purpose, and also used in the study of French et al. (1993).

2.2. 28 Sgr occultation

The 3 July 1989 occultation of the bright star 28 Sgr was widely observed, and provided the first post-*Voyager* occultation profiles of Saturn's rings. By combining the *Voyager* and 28 Sgr results, F93 measured the precession of Saturn's pole for the first time, and greatly improved upon the Saturn pole solution and absolute radius scale obtained from *Voyager* data alone (Simpson et al., 1983; Nicholson et al., 1990). The large projected diameter of the occultation star ($\sim$ 18 km) substantially smoothed many of the intrinsically sharper features that we use in our study. For a sharp step function in intrinsic ring optical depth, convolution of the point-source response with the strip brightness distribution of the occultation star is a symmetrical process that does not result in any bias in the fitted midpoint of the observed occultation profile compared to the actual location of the sharp ring edge. However, when the underlying ring structure has a gradual ramp-like variation in optical depth, there are instances where the fitted locations of a ring edge in observations that include the smoothing effects of the finite stellar disk are systematically biased from what would be obtained by a logistic fit to the actual optical depth profile. We correct for this bias empirically by including a radial offset for the 28 Sgr data as a fitted parameter in a least squares fit for the orbital elements of a ring that also includes many *Cassini* observations. When the fitted radial offset for a particular ring is statistically significant and exceeds 0.1 km, we include this correction to the fitted locations for all of the 28 Sgr data for that ring. For some ring features, this correction is as large as 1 km; as we will show below, most of the systematic differences between the F93 radius scale and our current results are due to such biases resulting from the large projected diameter of 28 Sgr.

The SM includes our measurements of the 28 Sgr data used in this study. We exclude ring features 29 and 36, which we now know are density waves in the C ring that were unresolved in the 28 Sgr observations, and 28 Sgr measurements of nominally circular B ring features 72, 75, 76, 81, 82, and 83 that F93 excluded from their adopted fit for the pole and radius scale because of the larger measurement uncertainties for these high optical depth features (see Fig. 13, Fit 14 in Table IX, and Table X, F93).

2.3. HST *occultation observations*

We have included measurements from two *HST* stellar occultations by Saturn's rings in our analysis. The first is the 1991 October 2/3 occultation of GSC 6323-01396 that was observed using the High Speed Photometer instrument as part of *HST* program 1081. Elliot et al. (1993) incorporated these observations into a global solution for the radius scale and Saturn's pole direction that included the 28 Sgr observations but excluded the *Voyager* results. As described in F10, we performed a completely independent analysis of these observations, including both our own measurements of individual ring features and our determination of the event geometry, using the latest available *HST* ephemeris.

The second *HST* occultation occurred on 1995 November 21 as part of *HST* program 5824, using the Faint Object Spectrograph. The occulted star was GSC 5249-01240. Bosh et al. (2002) used these results as part of an analysis of Saturn's F ring, but in the absence of published individual ring event times, we again performed our own independent analysis of the event, as described in detail in F10. The fitted midtimes of the ring events have rather large uncertainties for both events (see Figs. 1 and 2 of F10), as we discuss below in Section 6; nevertheless, the 1995 event is particularly sensitive to the assumed precession rate of Saturn's pole (F10), due to its proximity to the terrestrial ring plane crossing in August 1995. Together, the two *HST* occultations provide a consistency check on our global orbit solution, and our ring measurements for both are included in the SM.

3. *Cassini* occultation observations

The preponderance of the data used in this study come from a large set of *Cassini* ring occultations observed with the VIMS, UVIS, and RSS instruments. We included only high-SNR events with spatial resolution of 1 km or better, and excluded occultations of binary stars when the two occultation signatures materially interfered with each other. We also eliminated several distant occultations with uncertain spacecraft trajectories, a few events with large projected diameters of the occulted star, and occultations with very low ring opening angle B, for which slight spacecraft trajectory errors are greatly magnified when converted to ring plane radius. The data sets used here are a superset of those used in Papers 1, 2, and 3, which were restricted to occultations that intersected at least four fiducial circular features within the C and B rings or the Cassini Division. Here, we augment the previous set of observations to include those that span only the A ring, in spite of the dearth of sharp-edged A ring fiducial features with accurate orbits. (The structure of the A ring is dominated by overlapping density waves, with only a handful of sharp-edged features, none of whose fitted orbits rival the accuracy of those in the other main rings.) By including these additional occultations, we significantly increase the number of occultation observations whose radius scale can be accurately established using our global orbit solution. This is potentially quite useful for studies of density waves in the A ring, where an accurate radius scale can be of significant value when estimating the relative phases of density waves in multiple occultation chords. We also include *Cassini* measurements of inner B ring features 73, 74, 75, 76, 78, 81, 82, and 83 for comparison with the F93 orbital radius estimates based on their adopted astrometric solution.

For each occultation, we fitted logistic model curves to every detectable sharp-edged ringlet or gap edge to determine the observed midtime of each ring event. In the case of a few unresolved narrow ringlets, we fitted Gaussian, Lorentzian, or Voigt profiles, depending on the detailed shape of the feature. For RSS observations, the observed time refers to the instant that the spacecraft signal was received at the DSN receiving station on the Earth; for spacecraft stellar occultations, the observed time corresponds to the spacecraft event time (SCET) at which the signal was received on the spacecraft. The full set of 236 *Cassini* ingress or egress occultation chords used in this study is given in Table 1, listed separately for VIMS, UVIS, and RSS and alphabetically ordered within

[1] The diffraction-corrected *Voyager 1* RSS profiles are available from NASA's Planetary Data System Ring-Moon Systems Node (https://pds.jpl.nasa.gov/).

Table 1
Cassini occultation data.

Date	Event	$B(^\circ)$	r_{min} (km)[a],[b]	r_{max} (km)[c]	r'_{min} (km)[d]	r'_{max} (km)[e]	Δt (s)[f]	α[f],[g]	Δr_{max}[h] Δr_{min}[h]	N	rms (km)
2013 JUL 08	VIMS_2Cen194E	40.73	70000	128264	79222	120316	-0.013 ± 0.004		0.046	47	0.23
					79222	120316	-0.035 ± 0.008		-0.019	42	0.15
2013 JUL 08	VIMS_2Cen194I	40.73	70000	150000	74490	136522	0.089 ± 0.004	-0.0042 ± 0.0013	0.006	76	0.45
					74615	120316	0.093 ± 0.006		-0.094	44	0.14
2008 JUN 03	VIMS_CWLeo070E	-11.38	105664	140868	117787	136523	0.454 ± 0.008			16	1.38
2008 JUN 03	VIMS_CWLeo070I	-11.38	105664	148978	117913	136522	0.259 ± 0.009			15	0.90
2013 JUN 01	VIMS_RCar191I	63.48	70153	146983	74898	136520	0.108 ± 0.003	-0.0046 ± 0.0013		71	0.36
2008 APR 21	VIMS_RCas065I	-56.04	70000	138303	74899	136521	-0.003 ± 0.002		0.001	83	0.55
					75988	120315	-0.002 ± 0.002		0.000	48	0.18
2009 MAR 22	VIMS_RCas106I	-56.04	80338	145944	84751	136524	-0.049 ± 0.004		-0.023	86	0.29
					84751	120316	-0.049 ± 0.006		-0.025	53	0.16
2013 APR 01	VIMS_RCas185I	-56.04	70000	144996	74899	136521	0.156 ± 0.005	-0.0071 ± 0.0012	0.003	72	0.41
					75845	120316	0.149 ± 0.007	-0.0050 ± 0.0016	-0.055	46	0.15
2013 MAY 29	VIMS_RCas191I	-56.04	70000	146258	74943	136525	0.160 ± 0.004	-0.0044 ± 0.0014	0.061	70	0.52
					75989	120316	0.163 ± 0.005		-0.106	45	0.17
2013 JUN 10	VIMS_RCas192I	-56.04	102698	145962	133423	136524	0.103 ± 0.087			3	0.71
2013 JUL 05	VIMS_RCas194E	-56.04	71376	148290	74898	133745	0.017 ± 0.004		-0.006	78	0.45
					76043	120316	0.007 ± 0.006		-0.034	45	0.17
2013 APR 12	VIMS_RDor186I	56.27	115196	145116	117789	136524	0.068 ± 0.013		-0.066	21	0.43
					118629	120316	0.034 ± 0.022		-0.082	4	0.08
2013 MAY 01	VIMS_RDor188E	56.27	114972	149649	117775	133743	-0.045 ± 0.012		-0.096	20	0.57
					118628	120316	-0.015 ± 0.021		-0.117	4	0.06
2013 MAY 01	VIMS_RDor188I	56.27	114972	143226	117907	136523	0.083 ± 0.012		-0.095	22	0.45
					118628	120316	0.040 ± 0.021		-0.116	4	0.05
2007 JAN 01	VIMS_RHya036I	29.41	70000	150000	74490	136523	0.004 ± 0.003	0.0092 ± 0.0013	0.083	101	0.63
					75845	120316	0.006 ± 0.005	0.0128 ± 0.0017	-0.077	55	0.17
2007 MAR 29	VIMS_RHya041I	29.41	91469	144191	92377	136522	-0.011 ± 0.008	0.0161 ± 0.0025	-0.000	53	1.08
					92377	120316	-0.012 ± 0.011	0.0148 ± 0.0045	-0.043	27	0.17
2013 APR 04	VIMS_RHya185E	29.41	95301	136248	99363	133745	-0.043 ± 0.005		0.012	52	0.43
					99363	120316	-0.040 ± 0.008		-0.070	35	0.12
2013 APR 04	VIMS_RHya185I	29.41	95301	148120	99363	136522	-0.074 ± 0.008		0.023	44	0.35
					99363	120316	-0.058 ± 0.015		-0.046	28	0.19
2006 OCT 12	VIMS_RLeo030E	-9.55	109537	150000	117914	136522	0.022 ± 0.003			8	0.70
2006 OCT 12	VIMS_RLeo030I	-9.55	109537	150000	117807	136521	0.029 ± 0.003		0.048	18	0.61
					118629	120316	0.030 ± 0.004		0.044	4	0.19
2008 MAR 03	VIMS_RLeo060I	-9.55	126095	148125	133424	136522	0.049 ± 0.072			3	0.82
2008 MAR 14	VIMS_RLeo061E	-9.55	127918	146037	133424	136522	0.002 ± 0.081			3	0.72
2008 MAR 14	VIMS_RLeo061I	-9.55	127918	150000	133423	136522	0.163 ± 0.081			3	0.47
2008 APR 03	VIMS_RLeo063E	-9.55	114770	150000	117821	136523	0.043 ± 0.008			20	0.54
2008 APR 03	VIMS_RLeo063I	-9.55	114770	146139	117832	136523	0.068 ± 0.008		-0.003	23	0.75
					118629	120317	0.058 ± 0.014		-0.006	4	0.07
2008 MAY 19	VIMS_RLeo068E	-9.55	104095	150000	117898	133745	0.021 ± 0.007			9	0.86
2008 JUL 09	VIMS_RLeo075E	-9.55	104177	149999	117820	136523	0.081 ± 0.006		0.026	23	1.28
					118629	120316	0.066 ± 0.010		0.024	4	0.07

(*continued on next page*)

Table 1 (*continued*)

Date	Event	B(°)	r_{min} (km)[a],[b]	r_{max} (km)[c]	r'_{min} (km)[d]	r'_{max} (km)[e]	Δt (s)[f]	α[f],[g]	Δr_{max}[h] Δr_{min}[h]	N	rms (km)
2008 JUL 09	VIMS_RLeo075I	−9.55	104177	150000	117798	133745	0.130 ± 0.007			21	0.48
2008 JUL 23	VIMS_RLeo077E	−9.55	108281	150000	117787	136521	−0.024 ± 0.006		0.030	23	0.52
					118629	120316	−0.042 ± 0.011		0.027	4	0.04
2008 JUL 23	VIMS_RLeo077I	−9.55	108281	148320	117780	136522	0.013 ± 0.007		0.025	24	0.66
					118629	120316	0.002 ± 0.012		0.022	4	0.09
2008 SEP 27	VIMS_RLeo086E	−9.55	127256	149999	133423	136523	0.006 ± 0.077			3	1.06
2008 OCT 04	VIMS_RLeo087E	−9.55	128136	146309	133424	136522	0.011 ± 0.082			3	0.49
2008 OCT 04	VIMS_RLeo087I	−9.55	128136	149286	133424	136521	0.114 ± 0.082			3	0.38
2012 DEC 04	VIMS_RLyr176I	−40.78	106447	145956	117906	136521	−0.502 ± 0.031			10	0.71
2013 JAN 27	VIMS_RLyr180E	−40.78	108785	126227	117815	122050	0.612 ± 0.033		−0.125	20	0.60
					118628	120316	0.763 ± 0.058		−0.133	4	0.08
2013 JAN 26	VIMS_RLyr180I	−40.78	108785	149703	117819	136524	−0.468 ± 0.026		−0.066	22	0.61
					118629	120316	−0.494 ± 0.051		−0.069	4	0.08
2008 AUG 13	VIMS_RSCnc080E	−29.95	78000	143132	79222	133744	−0.013 ± 0.004		0.011	80	0.74
					79222	120316	−0.021 ± 0.006		−0.003	45	0.16
2008 AUG 13	VIMS_RSCnc080I	−29.95	78000	144260	79222	136522	0.084 ± 0.005		−0.008	85	0.81
					79222	120316	0.075 ± 0.007		−0.012	52	0.17
2008 SEP 19	VIMS_RSCnc085E	−29.95	81117	145603	84752	136525	−0.044 ± 0.004		0.013	81	0.65
					84752	120316	−0.052 ± 0.006		−0.000	46	0.16
2008 SEP 18	VIMS_RSCnc085I	−29.95	81117	144168	84752	136520	0.019 ± 0.005		−0.002	83	0.85
					84752	120316	0.011 ± 0.007		−0.006	48	0.15
2008 OCT 03	VIMS_RSCnc087E	−29.95	82502	143886	84751	136521	−0.025 ± 0.004		−0.014	80	0.63
					84751	120316	−0.028 ± 0.006		−0.027	45	0.15
2008 OCT 03	VIMS_RSCnc087I	−29.95	82502	144821	84752	133744	0.039 ± 0.005		−0.009	86	0.80
					84752	120316	0.030 ± 0.007		−0.011	51	0.14
2008 NOV 10	VIMS_RSCnc092I	−29.95	111362	142678	117839	136522	0.049 ± 0.011		−0.059	24	0.71
					118629	120317	0.024 ± 0.022		−0.063	4	0.07
2013 JAN 19	VIMS_WHya179I	34.65	70000	144370	74490	136520	0.065 ± 0.004		0.027	84	0.33
					74615	120316	0.074 ± 0.005		−0.069	48	0.12
2013 FEB 02	VIMS_WHya180I	34.65	70000	150000	74615	136522	0.064 ± 0.004		0.015	84	0.31
					74615	119406	0.071 ± 0.005		−0.085	46	0.13
2013 FEB 15	VIMS_WHya181I	34.65	70000	150000	74491	136521	0.010 ± 0.004		0.027	80	0.40
					75845	120316	0.019 ± 0.005		−0.067	44	0.12
2013 APR 13	VIMS_WHya186E	34.65	79888	150000	84752	133744	0.053 ± 0.004		0.027	62	0.36
					84752	119406	0.034 ± 0.006		−0.047	39	0.11
2013 MAY 12	VIMS_WHya189E	34.65	79064	150000	79222	133423	0.062 ± 0.004		0.013	61	0.49
					79222	119406	0.045 ± 0.006		−0.075	40	0.12
2013 AUG 17	VIMS_WHya196E	34.65	98396	141447	99363	133745	−0.027 ± 0.014	−0.0169 ± 0.0043	0.107	53	0.35
					99363	120316	−0.009 ± 0.017		−0.048	35	0.15
2013 AUG 17	VIMS_WHya196I	34.65	98396	142452	99363	136525	0.158 ± 0.013	−0.0240 ± 0.0045	0.165	48	0.61
					99363	118966	0.109 ± 0.011		−0.067	31	0.16
2013 SEP 10	VIMS_WHya197E	34.65	99425	124117	99576	122049	0.144 ± 0.018	0.0192 ± 0.0050	−0.005	49	0.51
					99576	120316	0.152 ± 0.026	0.0276 ± 0.0075	−0.029	35	0.11
2013 SEP 10	VIMS_WHya197I	34.65	99425	144620	99576	136522	−0.026 ± 0.016	0.0169 ± 0.0050	−0.009	51	0.42
					99576	120316	−0.059 ± 0.021	0.0252 ± 0.0076	−0.045	32	0.13
2007 MAR 23	VIMS_alpAur041I	−50.88	71910	143195	74490	133744	−0.049 ± 0.003	0.0049 ± 0.0011	0.032	107	0.41
					74615	120315	−0.050 ± 0.004	0.0067 ± 0.0015	−0.049	60	0.13
2009 MAY 09	VIMS_alpAur110E	−50.88	95401	145628	96889	136522	0.026 ± 0.007		0.090	59	0.33
					99363	120316	−0.025 ± 0.013	−0.0184 ± 0.0052	−0.151	36	0.09

(*continued on next page*)

Table 1 (*continued*)

Date	Event	B(°)	r_{min} (km)[a],[b]	r_{max} (km)[c]	r'_{min} (km)[d]	r'_{max} (km)[e]	Δt (s)[f]	α[f],[g]	Δr_{max}[h] Δr_{min}[h]	N	rms (km)
2009 MAY 09	VIMS_alpAur110I	−50.88	95401	144808	96889	136521	0.194 ± 0.007		0.020	58	0.44
					99363	120316	0.209 ± 0.011		−0.014	35	0.13
2012 JUN 28	VIMS_alpCMa168I	13.48	73673	91402	76262	90406	0.292 ± 0.002			13	0.16
2012 JUL 22	VIMS_alpCMa169I	13.48	71539	87308	76262	87292	0.262 ± 0.003			6	0.11
2006 JUL 23	VIMS_alpOri026I	−11.68	70001	150000	117781	133745	−0.001 ± 0.006			19	0.56
2009 AUG 27	VIMS_alpOri117I	−11.68	70000	143385	79222	133745	0.032 ± 0.002		−0.037	30	0.32
					79222	103779	0.028 ± 0.003		−0.052	25	0.19
2005 AUG 20	VIMS_alpSco013E	32.16	101172	146883	101190	136521	0.061 ± 0.004		0.041	50	0.41
					101190	120316	0.074 ± 0.008		−0.101	30	0.16
2005 AUG 20	VIMS_alpSco013I	32.16	101172	150000	101190	136520	0.046 ± 0.005		0.043	48	0.33
					101190	120316	0.034 ± 0.009		−0.048	30	0.14
2006 SEP 26	VIMS_alpSco029I	32.16	94689	149195	95371	136524	0.024 ± 0.005		−0.004	59	0.72
					99576	120316	0.022 ± 0.007		−0.008	35	0.12
2009 JUL 27	VIMS_alpSco115I	32.16	76063	144902	79263	136520	0.179 ± 0.008		−0.002	55	0.28
					79263	118967	0.187 ± 0.011		−0.014	47	0.11
2008 JAN 03	VIMS_alpSco55E	32.16	119783	141946	120232	133744	−0.087 ± 0.027			5	0.46
2008 JUL 28	VIMS_betGru078I	43.38	83914	142365	84752	133747	−0.028 ± 0.002		−0.009	82	0.50
					84752	120316	−0.031 ± 0.003		−0.019	49	0.13
2009 FEB 26	VIMS_betPeg104I	−31.68	73089	150000	74491	136524	0.027 ± 0.002		−0.014	104	0.55
					74615	120316	0.023 ± 0.003		−0.014	54	0.17
2009 APR 05	VIMS_betPeg108I	−31.68	84843	144915	85662	136523	0.037 ± 0.003		0.008	75	0.65
					85662	120316	0.036 ± 0.004		0.008	43	0.15
2012 AUG 11	VIMS_betPeg170E	−31.68	77201	137565	77350	136522	−0.165 ± 0.006	−0.0146 ± 0.0015	0.024	73	0.27
					77350	120316	−0.188 ± 0.010	−0.0163 ± 0.0022	−0.082	43	0.10
2012 SEP 22	VIMS_betPeg172I	−31.68	70000	144974	74491	136522	0.003 ± 0.005	0.0070 ± 0.0012	−0.006	93	0.46
					74615	120316	−0.006 ± 0.007	0.0072 ± 0.0017	−0.033	56	0.14
2008 NOV 23	VIMS_epsMus094E	72.77	104886	141218	118629	136522	−0.057 ± 0.017			8	0.39
2008 NOV 23	VIMS_epsMus094I	72.77	104886	143476	118629	136522	0.071 ± 0.016			8	0.18
2008 JUN 08	VIMS_gamCru071I	62.35	70000	144305	74491	136521	0.036 ± 0.003		−0.013	106	0.30
					74615	120316	0.034 ± 0.004		−0.014	58	0.12
2008 JUN 15	VIMS_gamCru072I	62.35	105938	144692	117792	136521	0.096 ± 0.005		−0.049	25	0.57
					118628	120316	0.089 ± 0.011		−0.049	4	0.02
2008 JUN 22	VIMS_gamCru073I	62.35	70000	144543	74491	136521	0.062 ± 0.003		−0.022	108	0.36
					74615	120316	0.058 ± 0.004		−0.023	59	0.10
2008 JUL 27	VIMS_gamCru078I	62.35	70000	144370	74491	133744	−0.024 ± 0.003		−0.012	101	0.23
					74615	120317	−0.026 ± 0.004		−0.012	57	0.12
2008 AUG 03	VIMS_gamCru079I	62.35	70000	148735	74490	136522	0.031 ± 0.003		−0.007	86	0.30
					74615	104083	0.029 ± 0.004		−0.007	56	0.10
2008 AUG 18	VIMS_gamCru081I	62.35	70000	146321	74615	133746	0.037 ± 0.003		−0.002	105	0.29
					74615	119406	0.037 ± 0.004		−0.002	59	0.10
2008 AUG 25	VIMS_gamCru082I	62.35	70000	149550	74615	136522	−0.024 ± 0.003		−0.014	107	0.39
					74615	120316	−0.026 ± 0.004		−0.014	58	0.11
2008 SEP 24	VIMS_gamCru086I	62.35	74580	143533	74615	136523	0.016 ± 0.003	−0.0029 ± 0.0011	0.058	109	0.34
					74615	120316	0.016 ± 0.004		−0.076	58	0.10
2008 OCT 16	VIMS_gamCru089I	62.35	70000	144132	74491	133745	0.012 ± 0.003		−0.003	113	0.33
					75845	120316	0.011 ± 0.004		−0.003	61	0.12
2008 NOV 15	VIMS_gamCru093I	62.35	70000	145271	74491	136521	−0.004 ± 0.004		−0.007	101	0.39
					75845	119406	−0.004 ± 0.005		−0.007	52	0.12
2008 NOV 23	VIMS_gamCru094I	62.35	70000	144259	74615	136523	−0.020 ± 0.003		−0.008	107	0.34
					74615	120316	−0.022 ± 0.004		−0.008	61	0.13

(*continued on next page*)

Table 1 (*continued*)

Date	Event	$B(^\circ)$	r_{min} (km)[a],[b]	r_{max} (km)[c]	r'_{min} (km)[d]	r'_{max} (km)[e]	Δt (s)[f]	α[f],[g]	Δr_{max}[h] Δr_{min}[h]	N	rms (km)
2008 DEC 08	VIMS_gamCru096I	62.35	70000	146904	74490	136523	0.015 ± 0.003		0.002	106	0.32
					74615	120316	0.015 ± 0.004		0.002	58	0.12
2008 DEC 16	VIMS_gamCru097I	62.35	95243	145803	98274	136522	0.039 ± 0.004		−0.006	56	0.52
					99363	120316	0.038 ± 0.005		−0.006	33	0.12
2009 JAN 12	VIMS_gamCru100I	62.35	70000	145973	74491	136521	−0.007 ± 0.003		−0.002	97	0.34
					74615	120316	−0.005 ± 0.004		−0.004	50	0.10
2009 JAN 21	VIMS_gamCru101I	62.35	70000	145909	74615	133746	0.004 ± 0.003		−0.006	106	0.49
					74615	120316	0.005 ± 0.004		−0.007	57	0.12
2009 JAN 31	VIMS_gamCru102I	62.35	70001	146977	74491	136521	0.003 ± 0.003	−0.0030 ± 0.0010	0.064	115	0.34
					74615	120316	0.006 ± 0.004		−0.075	62	0.12
2013 APR 22	VIMS_gamCru187E	62.35	70000	143382	74490	136524	0.015 ± 0.003		0.007	85	0.33
					74615	119406	0.009 ± 0.005		−0.025	51	0.14
2013 APR 22	VIMS_gamCru187I	62.35	70000	142134	74491	133422	0.051 ± 0.003	−0.0052 ± 0.0012	0.070	82	0.57
					75845	118967	0.049 ± 0.005		−0.124	49	0.15
2012 OCT 18	VIMS_lamVel173I	43.81	76048	146160	77864	136521	0.145 ± 0.003	−0.0084 ± 0.0017	0.166	59	0.52
					79222	120316	0.133 ± 0.004		−0.179	41	0.17
2013 MAR 31	VIMS_muCep185E	−59.90	71856	141875	74491	136523	−0.128 ± 0.006	−0.0137 ± 0.0012	0.024	88	0.39
					74615	120316	−0.129 ± 0.009	−0.0153 ± 0.0017	−0.069	55	0.14
2013 MAY 28,	VIMS_muCep191I	−59.90	70000	144861	74491	136523	0.146 ± 0.005	−0.0041 ± 0.0013	0.095	90	0.32
					74615	120316	0.143 ± 0.006		−0.094	55	0.14
2013 JUN 21	VIMS_muCep193I	−59.90	70001	146041	74615	136522	0.124 ± 0.005	−0.0042 ± 0.0012	0.095	94	0.31
					74615	120317	0.121 ± 0.006		−0.101	59	0.15
2013 JUL 03	VIMS_muCep194I	−59.90	113020	150000	117919	136520	0.061 ± 0.011			10	1.28
2013 JUL 15	VIMS_muCep195I	−59.90	106958	144758	117917	136520	0.263 ± 0.022			10	0.85
2006 NOV 09	UVIS_AlpAra032I	54.43	70000	139786	74899	136521	0.045 ± 0.004		−0.014	109	0.69
					75845	120316	0.042 ± 0.005		−0.015	63	0.12
2006 NOV 21	UVIS_AlpAra033I	54.43	70000	145356	74615	136521	0.089 ± 0.004		−0.039	110	0.35
					74615	120316	0.082 ± 0.005		−0.040	64	0.14
2006 DEC 17	UVIS_AlpAra035_2aI	54.43	86622	130426	74615	122051	0.159 ± 0.007		−0.003	90	0.46
					74615	120316	0.159 ± 0.009		−0.004	59	0.12
2007 JAN 05	UVIS_AlpAra036E	54.43	70897	115410	74491	104083	0.399 ± 0.008	0.0183 ± 0.0018	0.030	78	0.25
					77162	104083	0.405 ± 0.011	0.0165 ± 0.0022	−0.025	56	0.09
2007 JAN 04	UVIS_AlpAra036I	54.43	70897	113954	74490	104083	−0.086 ± 0.009	0.0183 ± 0.0015	0.014	88	0.34
					74615	104083	−0.094 ± 0.011	0.0175 ± 0.0017	−0.019	61	0.09
2008 APR 01	UVIS_AlpAra063E	54.43	73261	141565	74490	136524	0.022 ± 0.003		−0.003	101	0.56
					75989	120317	0.023 ± 0.004		−0.005	58	0.14
2008 APR 20	UVIS_AlpAra065E	54.43	125009	143857	133424	136522	−0.089 ± 0.062			3	0.66
2008 AUG 04	UVIS_AlpAra079I	54.43	94195	150000	94438	136522	0.011 ± 0.004		−0.024	60	0.37
					99363	120316	0.011 ± 0.006		−0.028	36	0.12
2008 SEP 17	UVIS_AlpAra085E	54.43	93510	150000	94439	136521	−0.022 ± 0.004		−0.014	62	0.51
					99363	120316	−0.020 ± 0.006		−0.017	38	0.12
2008 SEP 17	UVIS_AlpAra085I	54.43	93510	150000	94439	136525	0.001 ± 0.004		0.006	63	0.44
					99363	120316	0.006 ± 0.006		−0.006	39	0.09
2008 SEP 24	UVIS_AlpAra086E	54.43	93407	150000	94438	136523	0.008 ± 0.004		0.008	60	0.55
					99363	120316	0.007 ± 0.006		−0.005	37	0.12
2008 SEP 24	UVIS_AlpAra086I	54.43	93407	150000	94438	133746	0.034 ± 0.004		0.010	61	0.47
					99363	120316	0.040 ± 0.006		−0.004	38	0.13

(*continued on next page*)

Table 1 (*continued*)

Date	Event	$B(^\circ)$	r_{min} (km)[a],[b]	r_{max} (km)[c]	r'_{min} (km)[d]	r'_{max} (km)[e]	Δt (s)[f]	α[f],[g]	Δr_{max}[h] Δr_{min}[h]	N	rms (km)
2008 OCT 24	UVIS_AlpAra090E	54.43	92106	150000	92366	136522	-0.015 ± 0.004		0.001	64	0.53
					92366	120316	-0.015 ± 0.006		−0.018	41	0.13
2008 OCT 24	UVIS_AlpAra090I	54.43	92106	150000	92366	136520	0.022 ± 0.004		−0.009	65	0.40
					92366	120316	0.026 ± 0.006		−0.019	41	0.10
2008 DEC 09	UVIS_AlpAra096E	54.43	108169	150000	117778	136525	0.033 ± 0.009		0.032	21	0.71
					118629	120316	0.024 ± 0.016		0.028	4	0.11
2008 DEC 09	UVIS_AlpAra096I	54.43	108169	150000	117790	136522	0.000 ± 0.008		−0.022	21	0.52
					118628	120316	0.004 ± 0.016		−0.023	4	0.12
2008 DEC 25	UVIS_AlpAra098E	54.43	110536	150000	117794	136524	0.032 ± 0.012		0.024	22	0.59
					118628	120316	0.021 ± 0.022		0.019	4	0.05
2008 DEC 25	UVIS_AlpAra098I	54.43	110536	150000	117777	136522	0.026 ± 0.012		−0.021	22	0.56
					118629	120316	0.032 ± 0.022		−0.022	4	0.13
2009 MAR 08	UVIS_AlpAra105E	54.43	93917	143383	94439	136523	-0.030 ± 0.007		−0.010	62	0.38
					99363	120316	-0.030 ± 0.010		−0.021	38	0.10
2009 MAR 07	UVIS_AlpAra105I	54.43	93917	150000	94438	136522	0.188 ± 0.011	-0.0103 ± 0.0029	0.109	64	0.47
					99363	120316	0.174 ± 0.011		−0.075	39	0.14
2012 JUN 28	UVIS_AlpCMa168I	13.48	73191	108881	74491	90614	-0.350 ± 0.005	-0.0209 ± 0.0058	0.016	32	0.46
					76261	90614	-0.365 ± 0.007	-0.0275 ± 0.0072	−0.016	18	0.16
2012 JUL 22	UVIS_AlpCMa169I	13.48	70000	99319	74491	90614	0.524 ± 0.005	-0.0295 ± 0.0057	0.050	31	0.33
					76262	90614	0.507 ± 0.007	-0.0394 ± 0.0072	−0.033	17	0.14
2009 JUN 27	UVIS_AlpLup113I	53.85	83839	118956	84752	118629	0.215 ± 0.009	-0.0151 ± 0.0020	−0.006	77	0.43
					84752	118629	0.225 ± 0.012	-0.0167 ± 0.0026	−0.028	54	0.12
2012 NOV 19	UVIS_AlpLyr175I	−35.22	70853	142814	74898	136520	0.240 ± 0.009		0.031	88	0.61
					75989	120316	0.202 ± 0.016		−0.038	60	0.15
2005 MAY 21	UVIS_AlpVir008E	17.25	118978	141736	122050	136522	0.089 ± 0.035			4	0.86
2005 MAY 21,	UVIS_AlpVir008I	17.25	118978	141952	122051	136521	0.154 ± 0.035			4	1.47
2006 DEC 03	UVIS_AlpVir034E	17.25	74536	150000	74615	136521	0.021 ± 0.001		0.001	116	0.64
					74615	120315	0.022 ± 0.002		−0.034	65	0.16
2006 DEC 03	UVIS_AlpVir034I	17.25	74536	150000	74615	136520	0.019 ± 0.001		0.001	115	0.44
					74615	120316	0.018 ± 0.002		−0.032	66	0.14
2009 AUG 11	UVIS_AlpVir116I	17.25	103058	144567	103260	136522	-0.019 ± 0.005	-0.0082 ± 0.0032	0.089	34	0.29
					103260	120317	-0.027 ± 0.004		−0.055	12	0.11
2010 JAN 11	UVIS_AlpVir124E	17.25	70494	142431	74490	136521	-0.060 ± 0.003		0.019	94	0.49
					76262	120316	-0.070 ± 0.003		−0.045	57	0.15
2010 JUL 05	UVIS_AlpVir134I	17.25	72604	143682	74490	136521	0.024 ± 0.002		0.010	94	0.55
					76262	120316	0.025 ± 0.003		−0.085	57	0.16
2012 OCT 19	UVIS_AlpVir173E	17.25	109357	143407	117785	133744	0.104 ± 0.007		−0.050	19	0.53
					118629	120316	0.118 ± 0.013		−0.064	4	0.10
2012 OCT 19	UVIS_AlpVir173I	17.25	109357	147211	117799	136523	-0.023 ± 0.013			14	0.21
2008 APR 10	UVIS_BetCen064E	66.72	84952	150000	85662	136522	0.000 ± 0.007		−0.013	90	0.46
					85662	120316	0.004 ± 0.010		−0.018	55	0.11
2008 JUL 06	UVIS_BetCen075I	66.72	72427	144448	74491	136520	0.075 ± 0.003		−0.016	116	0.32
					74615	120316	0.073 ± 0.004		−0.016	67	0.13
2008 JUL 20	UVIS_BetCen077_1I	66.72	73333	144893	74615	136521	-0.022 ± 0.003		−0.001	117	0.40
					74615	120316	-0.022 ± 0.004		−0.003	67	0.12
2008 JUL 21	UVIS_BetCen077_2E	66.72	73268	143447	74490	136522	-0.043 ± 0.003		−0.006	119	0.46
					74615	120316	-0.043 ± 0.004		−0.008	67	0.13
2008 JUL 28	UVIS_BetCen078E	66.72	70000	145024	74491	136523	-0.049 ± 0.003		−0.008	118	0.42
					74615	120316	-0.048 ± 0.004		−0.010	67	0.11

(*continued on next page*)

Table 1 (*continued*)

Date	Event	$B(^\circ)$	r_{min} (km)[a],[b]	r_{max} (km)[c]	r'_{min} (km)[d]	r'_{max} (km)[e]	Δt (s)[f]	α[f],[g]	Δr_{max}[h] Δr_{min}[h]	N	rms (km)
2008 AUG 18	UVIS_BetCen081I	66.72	72829	150000	74491	136522	0.025 ± 0.003		−0.018	121	0.43
					74615	120316	0.023 ± 0.004		−0.018	67	0.08
2008 SEP 16	UVIS_BetCen085I	66.72	73111	143414	74490	136523	−0.015 ± 0.003		−0.018	118	0.36
					74615	120316	−0.018 ± 0.004		−0.018	66	0.10
2008 OCT 16	UVIS_BetCen089I	66.72	71853	141886	74490	133745	0.005 ± 0.003		−0.010	119	0.43
					74615	120316	0.004 ± 0.004		−0.012	66	0.10
2008 NOV 08	UVIS_BetCen092E	66.72	70000	150000	74491	136522	0.006 ± 0.003		−0.006	118	0.49
					74615	120316	0.007 ± 0.004		−0.007	67	0.14
2008 DEC 08	UVIS_BetCen096I	66.72	72455	150000	74490	136521	0.017 ± 0.003		−0.014	120	0.36
					74615	120316	0.015 ± 0.004		−0.015	67	0.12
2009 JAN 31	UVIS_BetCen102I	66.72	73242	143508	74491	136522	0.002 ± 0.003		−0.005	120	0.38
					74615	120316	0.001 ± 0.004		−0.005	67	0.11
2009 FEB 23	UVIS_BetCen104E	66.72	70000	131988	74491	122053	0.014 ± 0.005		−0.020	117	0.44
					74615	120316	0.017 ± 0.006		−0.021	67	0.10
2009 FEB 22	UVIS_BetCen104I	66.72	70203	147291	74491	136523	−0.010 ± 0.004		−0.022	119	0.36
					74615	120316	−0.012 ± 0.006		−0.024	67	0.11
2009 MAR 06	UVIS_BetCen105_1I	66.72	88502	150000	88593	136522	−0.039 ± 0.005		−0.012	83	0.54
					88593	120316	−0.039 ± 0.006		−0.014	50	0.08
2009 MAR 07	UVIS_BetCen105_2E	66.72	77787	147359	77860	136522	0.044 ± 0.005		−0.019	96	0.40
					79222	120316	0.048 ± 0.006		−0.020	58	0.12
2008 DEC 24	UVIS_BetCru098I	65.18	70000	150000	74490	136521	−0.079 ± 0.003		−0.011	116	0.42
					74615	120316	−0.079 ± 0.004		−0.012	67	0.11
2009 JAN 22	UVIS_BetCru101I	65.18	74900	86105	74943	85924	−0.073 ± 0.007		−0.051	28	0.40
					75845	85924	−0.081 ± 0.008		−0.055	14	0.14
2013 APR 24	UVIS_BetLib187E	15.77	125892	145618	133423	136523	−0.592 ± 0.094			3	0.26
2008 JAN 26	UVIS_BetLup057I	49.58	119418	148147	120316	136522	0.032 ± 0.018			5	0.49
2009 JUL 12	UVIS_BetLup114I	49.58	118474	144836	118628	136523	−0.240 ± 0.068		−0.020	9	0.94
					118628	120316	−0.194 ± 0.107		−0.042	4	0.22
2007 APR 08	UVIS_BetPer042I	−47.37	84460	149674	84752	136522	−0.009 ± 0.002		−0.014	85	0.39
					84752	120316	−0.009 ± 0.002		−0.016	53	0.13
2008 APR 28	UVIS_DelCen066I	55.58	130072	143054	133424	136522	0.542 ± 0.450			3	0.76
2008 MAY 16,	UVIS_DelCen068I	55.58	124551	150000	133423	136522	−0.049 ± 0.092			3	0.98
2008 DEC 24	UVIS_DelCen098I	55.58	70000	150000	74615	136522	−0.122 ± 0.003		0.007	112	0.44
					74615	120316	−0.120 ± 0.004		0.007	64	0.16
2013 MAR 11	UVIS_DelCen183E	55.58	70000	146451	75989	136520	−0.376 ± 0.003		−0.010	58	0.41
					75989	104083	−0.382 ± 0.004		−0.031	43	0.16
2013 APR 03	UVIS_DelCen185E	55.58	70000	144162	74898	136522	−0.483 ± 0.003	0.0041 ± 0.0017	0.099	61	0.38
					76043	118967	−0.491 ± 0.004		−0.107	42	0.16
2013 JUN 02	UVIS_DelCen191E	55.58	70000	144575	74943	136522	−0.665 ± 0.003		−0.004	67	0.44
					76262	118629	−0.673 ± 0.004		−0.033	47	0.17
2013 JUL 08	UVIS_DelCen194I	55.58	87602	145907	88593	136522	−0.803 ± 0.003		−0.046	53	0.30
					88593	120316	−0.804 ± 0.004		−0.068	40	0.14
2008 JAN 26	UVIS_DelLup057I	47.01	114918	147965	117793	136523	0.036 ± 0.007		0.041	24	0.59
					118628	120316	0.044 ± 0.013		0.041	4	0.03

(*continued on next page*)

Table 1 (*continued*)

Date	Event	B(°)	r_{min} (km)[a],[b]	r_{max} (km)[c]	r'_{min} (km)[d]	r'_{max} (km)[e]	Δt (s)[f]	α[f],[g]	Δr_{max}[h] Δr_{min}[h]	N	rms (km)
2006 DEC 30	UVIS_DelPer036E	−53.99	70000	140902	76044	136524	0.036 ± 0.002			77	0.49
2007 JAN 15	UVIS_DelPer037I	−53.99	70000	142584	74615	136522	0.037 ± 0.003	0.0049 ± 0.0013	0.096	102	0.39
					74615	119406	0.033 ± 0.004		−0.129	61	0.16
2007 FEB 18	UVIS_DelPer039I	−53.99	70000	143283	74943	136521	0.031 ± 0.003	0.0053 ± 0.0013	0.102	97	0.43
					75989	120316	0.028 ± 0.004		−0.134	60	0.15
2007 MAR 23	UVIS_DelPer041I	−53.99	70000	149745	74899	136522	0.021 ± 0.002	0.0039 ± 0.0015	0.051	85	0.51
					76262	104083	0.017 ± 0.003		−0.059	50	0.17
2008 MAR 02	UVIS_DelPer060I	−53.99	70000	146216	74898	136523	0.037 ± 0.002		−0.016	83	0.49
					75989	104083	0.036 ± 0.002		−0.016	50	0.18
2012 OCT 18	UVIS_EpsCMa173I	25.99	75579	146082	76261	122050	0.086 ± 0.002	0.0180 ± 0.0014	0.114	82	0.51
					76261	120316	0.088 ± 0.003	0.0208 ± 0.0022	−0.083	54	0.14
2012 NOV 11	UVIS_EpsCMa174I	25.99	75743	146484	75807	136523	−0.008 ± 0.002		0.003	97	0.54
					75845	120316	−0.011 ± 0.003		−0.054	62	0.16
2008 APR 19	UVIS_EpsCen065I	59.65	70000	148191	75959	136521	0.049 ± 0.004		−0.008	107	0.38
					75989	120316	0.048 ± 0.005		−0.009	63	0.12
2007 JAN 03	UVIS_EpsLup036E	51.04	70000	148844	74615	136521	0.178 ± 0.004			111	0.50
2007 JAN 20	UVIS_EpsLup037E	51.04	99479	142940	99576	136523	0.743 ± 0.031	0.0471 ± 0.0058		39	0.28
2007 JAN 20	UVIS_EpsLup037I	51.04	99479	129589	99576	122050	−0.506 ± 0.032	0.0637 ± 0.0053		38	0.14
2007 FEB 14	UVIS_EpsPsA039I	23.72	86909	94012	87343	92377	−0.118 ± 0.016		−0.026	16	0.27
					88593	92377	−0.131 ± 0.020		−0.044	8	0.13
2006 DEC 03	UVIS_EtaLup034E	44.45	106848	143846	117830	136522	0.071 ± 0.011		−0.038	23	0.59
					118628	120316	0.083 ± 0.022		−0.040	4	0.10
2006 DEC 03	UVIS_EtaLup034I	44.45	106848	135360	117828	133744	0.013 ± 0.011		0.009	23	0.48
					118629	120316	0.015 ± 0.022		0.009	4	0.11
2007 JAN 22	UVIS_GamAra037_1I	61.00	121466	147952	122051	136522	0.372 ± 0.132			4	0.92
2007 JAN 22	UVIS_GamAra037_2E	61.00	80500	150000	84752	136521	−0.084 ± 0.007	−0.0064 ± 0.0015	0.015	88	0.37
					84752	120316	−0.079 ± 0.009	−0.0082 ± 0.0022	−0.050	55	0.10
2007 FEB 10	UVIS_GamAra038I	61.00	87183	93028	87292	92453	0.676 ± 0.017		−0.036	20	0.33
					87292	92453	0.657 ± 0.021		−0.043	12	0.13
2008 APR 11	UVIS_GamCas064I	−66.35	71733	119601	74615	119406	0.007 ± 0.002		−0.024	97	0.48
					74615	119407	0.006 ± 0.002		−0.027	64	0.15
2009 JAN 15	UVIS_GamCas100E	−66.35	72440	140370	74899	136523	−0.003 ± 0.003		−0.013	109	0.57
					75845	120316	−0.001 ± 0.004		−0.014	63	0.14
2007 MAR 21	UVIS_GamGru041E	35.14	91526	142230	92395	136523	0.170 ± 0.006		−0.019	60	0.54
					92395	119406	0.185 ± 0.008		−0.078	36	0.16
2007 MAR 21	UVIS_GamGru041I	35.14	91526	145956	92377	136520	−0.115 ± 0.008	0.0217 ± 0.0027	0.074	66	0.46
					92377	120315	−0.123 ± 0.009	0.0272 ± 0.0042	−0.052	41	0.16
2006 DEC 29	UVIS_GamPeg036E	−20.29	102296	146797	102455	136525	−0.288 ± 0.043	−0.1228 ± 0.0167	0.072	37	0.73
					102455	120316	−0.345 ± 0.057	−0.1434 ± 0.0231	−0.003	17	0.20
2006 DEC 29	UVIS_GamPeg036I	−20.29	102296	150000	102455	136526	0.457 ± 0.042	−0.1247 ± 0.0167	0.054	36	0.78
					102455	120316	0.516 ± 0.056	−0.1507 ± 0.0231	−0.077	16	0.16
2012 SEP 23	UVIS_GamPeg172E	−20.29	126305	142395	133421	136524	−0.080 ± 0.149			3	1.86
2012 SEP 23	UVIS_GamPeg172I	−20.29	126304	137986	133423	136523	−0.036 ± 0.150			3	0.18
2006 DEC 17	UVIS_KapCen035E	48.55	70000	146177	74615	136522	−0.002 ± 0.005		−0.006	114	0.41
					74615	120316	−0.001 ± 0.006		−0.010	66	0.14
2007 JAN 02	UVIS_KapCen036I	48.55	70000	150000	74615	136521	0.056 ± 0.004		−0.013	115	0.36
					74615	120316	0.054 ± 0.006		−0.015	66	0.12

(*continued on next page*)

Table 1 (*continued*)

Date	Event	$B(^\circ)$	r_{min} (km)[a],[b]	r_{max} (km)[c]	r'_{min} (km)[d]	r'_{max} (km)[e]	Δt (s)[f]	α[f],[g]	Δr_{max}[h] Δr_{min}[h]	N	rms (km)
2007 APR 02	UVIS_KapCen042E	48.55	114712	127824	117823	122050	-0.703 ± 0.044		-0.027	22	0.34
					118629	120316	-0.670 ± 0.088		-0.031	4	0.03
2013 MAR 10	UVIS_KapVel183E	55.61	70000	126626	76262	122049	-0.358 ± 0.002		-0.015	58	0.49
					76262	104083	-0.353 ± 0.003		-0.020	44	0.16
2006 SEP 27	UVIS_LamSco029E	41.70	88478	143805	88592	133744	-2.041 ± 0.010	-0.0097 ± 0.0021	0.150	80	0.36
					88592	120316	-2.023 ± 0.012		-0.108	48	0.12
2007 MAY 09	UVIS_LamSco044I	41.70	74500	141063	74615	136522	0.055 ± 0.005	-0.0053 ± 0.0010	0.101	118	0.43
					74615	120316	0.055 ± 0.007		-0.140	67	0.12
2009 JUL 14	UVIS_LamSco114I	41.70	110857	148227	117853	136522	-0.675 ± 0.033		-0.043	24	0.35
					118629	120316	-0.678 ± 0.066		-0.046	4	0.08
2009 JUN 26	UVIS_MuCen113I	48.75	75975	150000	75988	136522	-0.007 ± 0.004	0.0047 ± 0.0013	0.076	97	0.39
					75988	120316	-0.014 ± 0.005		-0.130	60	0.17
2009 AUG 27	UVIS_Pi4Ori117E	-11.06	70000	145303	76043	136524	-0.017 ± 0.002			36	0.62
2005 JUL 14	UVIS_SigSgr011I	29.05	85971	146929	86373	133745	0.017 ± 0.002		-0.030	83	0.47
					86373	120316	0.009 ± 0.003		-0.056	51	0.15
2009 JUL 17	UVIS_SigSgr114I	29.05	84450	149876	92366	136521	0.443 ± 0.010		-0.026	70	0.38
					92366	120316	0.440 ± 0.014		-0.027	43	0.13
2013 MAY 21	UVIS_TheCar190I	67.00	72291	145557	75989	136523	-0.569 ± 0.003		-0.002	72	0.67
					75989	118967	-0.573 ± 0.004		-0.010	51	0.15
2012 JUL 23	UVIS_ZetCMa169E	26.18	121733	145664	122053	136524	0.164 ± 0.070			4	2.16
2012 JUL 22	UVIS_ZetCMa169I	26.18	121733	149999	122048	136523	0.241 ± 0.071			4	1.12
2008 FEB 29	UVIS_ZetCen060I	53.60	70000	146507	74899	133745	0.009 ± 0.004		-0.020	112	0.34
					75846	120316	0.006 ± 0.006		-0.021	64	0.10
2008 MAR 22	UVIS_ZetCen062E	53.60	70000	145087	74491	136522	0.014 ± 0.005		-0.009	114	0.34
					75846	120317	0.016 ± 0.006		-0.010	65	0.13
2009 JUN 12	UVIS_ZetCen112I	53.60	71486	143214	74615	133746	0.011 ± 0.005		-0.018	109	0.38
					74615	120316	0.007 ± 0.006		-0.019	65	0.11
2007 APR 08	UVIS_ZetPer042E	-38.01	132811	137957	133423	136521	0.143 ± 0.280			3	0.39
2012 SEP 03	UVIS_ZetPup171E	38.63	86532	145478	87292	136523	0.110 ± 0.004	-0.0253 ± 0.0020	0.001	69	0.29
					87292	120316	0.111 ± 0.005	-0.0226 ± 0.0032	-0.044	45	0.16
2012 SEP 03	UVIS_ZetPup171I	38.63	86532	144270	92366	133744	0.306 ± 0.005	-0.0135 ± 0.0028	0.032	53	0.21
					92366	120316	0.287 ± 0.007	-0.0182 ± 0.0051	-0.114	37	0.09
2005 MAY 03	RSS_007E_X43	-23.57	72761	144999	74490	136522	0.070 ± 0.002	0.0069 ± 0.0011	0.151	119	0.46
					74615	120316	0.071 ± 0.003		-0.171	66	0.16
2005 MAY 03	RSS_007I_X43	-23.58	72001	144999	74491	136520	-0.021 ± 0.002		0.017	117	0.50
					74615	120316	-0.021 ± 0.002		0.012	66	0.14
2005 MAY 21,	RSS_008E_X63	-23.17	73811	144999	74491	136522	0.090 ± 0.002	0.0052 ± 0.0011	0.113	120	0.36
					74614	120316	0.090 ± 0.003		-0.131	67	0.14
2005 MAY 21,	RSS_008I_X43	-23.17	73854	144999	74491	136522	-0.009 ± 0.002	0.0050 ± 0.0011	0.105	116	0.60
					74615	120316	-0.011 ± 0.002		-0.129	66	0.13
2005 JUN 08	RSS_009E_X14	-22.64	72812	144999	74491	136519	-0.001 ± 0.002		-0.017	116	0.52
					74615	120315	-0.000 ± 0.003		-0.022	64	0.15
2005 JUN 27	RSS_010E_X14	-22.00	72001	144999	74491	136520	-0.006 ± 0.002	-0.0033 ± 0.0011	0.057	116	0.48
					74615	120316	-0.006 ± 0.003		-0.090	64	0.17
2005 JUN 26	RSS_010I_X14	-22.01	72001	144999	74490	136523	0.016 ± 0.002		-0.007	119	0.44
					74615	120316	0.015 ± 0.002		-0.012	66	0.13
2005 JUL 15	RSS_011E_X43	-21.29	72250	118300	74899	118284	0.003 ± 0.002		-0.009	88	0.50
					75989	104083	0.003 ± 0.003		-0.013	56	0.15

(*continued on next page*)

Table 1 (*continued*)

Date	Event	$B(^\circ)$	r_{min} (km)[a],[b]	r_{max} (km)[c]	r'_{min} (km)[d]	r'_{max} (km)[e]	Δt (s)[f]	α[f],[g]	Δr_{max}[h] Δr_{min}[h]	N	rms (km)
2005 JUL 15	RSS_011E_X63	−21.29	82691	144999	84752	136522	0.004 ± 0.002		−0.009	85	0.55
					84752	120317	0.004 ± 0.003		−0.013	54	0.16
2005 AUG 02	RSS_012E_X63	−20.53	72001	144999	74491	136524	−0.003 ± 0.002		−0.012	114	0.52
					74615	120316	−0.003 ± 0.003		−0.020	63	0.15
2005 AUG 02	RSS_012I_X63	−20.54	72001	144999	74490	136521	0.014 ± 0.002		0.005	112	0.48
					74615	120316	0.016 ± 0.003		−0.003	63	0.16
2005 AUG 20	RSS_013E_X14	−19.76	72001	144999	74490	136522	−0.011 ± 0.002		0.010	119	0.41
					74615	120316	−0.012 ± 0.002		0.000	66	0.14
2005 SEP 05	RSS_014I_X14	−19.12	72001	144999	74491	136520	0.000 ± 0.002		0.015	119	0.34
					74615	120316	−0.001 ± 0.003		−0.011	64	0.12
2007 MAY 10,	RSS_044E_X63	−15.22	72001	144999	74490	136520	0.000 ± 0.002		−0.009	111	0.31
					74615	120316	0.002 ± 0.002		−0.021	61	0.16
2007 JUN 11	RSS_046I_X14	−14.37	72001	144999	74490	136523	0.002 ± 0.002	−0.0027 ± 0.0011	0.051	113	0.42
					74615	120316	0.001 ± 0.002		−0.088	61	0.15
2007 DEC 03	RSS_053I_X63	−6.68	101861	144999	117786	136520	0.002 ± 0.002		0.006	26	0.62
					118629	120316	0.001 ± 0.004		0.000	4	0.10
2007 DEC 19	RSS_054E_X63	−6.63	89151	140104	89190	136522	−0.011 ± 0.002		−0.003	32	0.91
					89190	120316	−0.011 ± 0.003		−0.047	9	0.11
2007 DEC 19	RSS_054I_X63	−6.63	88761	144999	89190	136521	0.000 ± 0.001		−0.014	46	0.32
					89190	120317	−0.003 ± 0.002		−0.051	22	0.14
2008 JAN 15	RSS_056E_X63	−7.04	74201	141588	74491	136523	−0.007 ± 0.001	0.0036 ± 0.0011	0.062	71	0.59
					74615	120316	−0.007 ± 0.001		−0.074	27	0.18
2008 JAN 15	RSS_056I_X63	−7.04	74201	144999	74491	136523	0.003 ± 0.001		0.004	73	0.32
					74615	120316	0.000 ± 0.001		−0.039	26	0.16
2008 JAN 27	RSS_057E_X43	−7.38	74101	138405	74491	136523	−0.006 ± 0.001	0.0060 ± 0.0011	0.120	70	0.56
					74615	120316	−0.006 ± 0.001		−0.144	26	0.14
2008 JAN 27	RSS_057I_X43	−7.38	74101	144999	74491	136523	0.006 ± 0.001		0.081	77	0.42
					74615	120316	0.004 ± 0.001		−0.016	30	0.14
2008 FEB 08	RSS_058E_X43	−7.80	72001	108880	74490	102232	−0.004 ± 0.001		0.052	49	0.31
					74615	102232	−0.005 ± 0.001		−0.006	23	0.14
2008 FEB 08	RSS_058I_X43	−7.80	72001	144999	74491	136523	0.007 ± 0.001	0.0022 ± 0.0012	0.032	78	0.66
					74615	120316	0.005 ± 0.001		−0.007	32	0.16
2008 MAR 02	RSS_060E_X14	−8.65	72001	138375	74490	136522	−0.009 ± 0.001	0.0055 ± 0.0011	0.109	74	0.35
					74614	120316	−0.009 ± 0.001		−0.105	28	0.17
2008 MAR 02	RSS_060I_X14	−8.65	72001	144999	74491	136523	0.003 ± 0.001		0.048	83	0.47
					74615	120317	0.001 ± 0.001		−0.014	34	0.13
2008 APR 01	RSS_063E_X63	−9.60	72001	144999	74491	136523	−0.009 ± 0.001	0.0039 ± 0.0011	0.068	74	0.41
					74614	120316	−0.009 ± 0.001		−0.088	27	0.15
2008 APR 01	RSS_063I_X63	−9.60	72001	144999	74491	136520	0.003 ± 0.001		0.012	87	0.47
					74615	120316	0.001 ± 0.001		−0.023	39	0.13
2008 APR 11	RSS_064E_X43	−9.79	72001	144999	74491	136522	−0.007 ± 0.001		−0.023	72	0.91
					74615	120316	−0.008 ± 0.001		−0.043	28	0.10
2008 APR 11	RSS_064I_X43	−9.79	72001	144999	74490	136520	0.005 ± 0.001		−0.004	85	0.46
					74615	120316	0.002 ± 0.001		−0.031	36	0.12

(*continued on next page*)

Table 1 (*continued*)

Date	Event	B(°)	r_{min} (km)[a],[b]	r_{max} (km)[c]	r'_{min} (km)[d]	r'_{max} (km)[e]	Δt (s)[f]	α[f],[g]	Δr_{max}[h] Δr_{min}[h]	N	rms (km)
2008 MAY 10	RSS_067E_X14	−9.91	72001	144999	74490	136520	−0.005 ± 0.001	0.0038 ± 0.0011	0.041	69	0.67
					74615	120316	−0.005 ± 0.001	−0.0050 ± 0.0016	−0.134	26	0.15
2008 MAY 09	RSS_067I_X14	−9.91	72001	144999	74491	136523	0.005 ± 0.001		0.010	82	0.33
					74615	120316	0.002 ± 0.001		−0.025	37	0.14
2009 DEC 25	RSS_123I_X43	4.83	74000	78000	74615	77876	0.431 ± 0.157	0.1692 ± 0.0663	−0.036	12	0.14
					74615	77348	0.465 ± 0.150		−0.061	8	0.14
2010 JAN 26	RSS_125I_X43	4.76	74000	78000	74615	77873	0.845 ± 0.152	0.3311 ± 0.0663	0.110	12	0.33
					74615	77348	0.728 ± 0.145		−0.060	8	0.15

(a) For stellar occultations: AAAA_BBBNNND, where AAAA=VIMS or UVIS, BBB= star name, NNN=rev number, direction D=I or E, for ingress or egress. For RSS occultations: RSS_NNND_BZZ, where NNN=rev number, D= I or E for ingress or egress, B=transmitted band (X for X-band), and ZZ = DSN number (ex: 14=DSS14)
(b) Minimum ring plane radius sampled by event
(c) Maximum ring plane radius sampled by event
(d) Minimum radius of fitted features used to determine correction factors Δt and α. The first row for each event is for Fit #7; the second row, when present, is for Fit #1.
(e) Maximum radius of fitted features used to determine correction factors Δt and α
(f) First row: Fit #7; second row (when present): Fit #1 (see Table 4)
(g) See Eq. (4)
(h) For a given event, $\Delta r_{max,min}$ are the maximum/minimum differences (Fit #7 - Fit #1) in the measured radii of fitted features in common between the two fits.

each set. Included in the table are the event date and name, the ring opening angle B, the minimum and maximum equatorial radius sampled by the occultation chord (r_{min} and r_{max}, respectively), and additional quantities to be defined later.

The combined set of *Cassini* observations enables substantial improvements in the determination of orbits for ring features in several ways. The sheer abundance of events results in typical ring features having 100–200 individual high-SNR measurements over a large range of orbital longitudes and spanning more than a decade in time, making it possible to detect complex orbital kinematics such as multiple free and forced normal modes and inclinations with amplitudes as small as 0.1 km in radius and 0.2 km in $a\sin i$, and to measure pattern speeds with uncertainties as small as $1^\circ \mathrm{cy}^{-1}$ in some cases. The wide range of ring opening angles and viewing geometries also tightly constrains both the radius scale of the rings and the direction of Saturn's pole, decoupling the strong correlations between ring radius and pole direction implicit in most single-occultation events.

Fig. 1 illustrates the variety of observed occultation chord geometries by showing a polar projection of the Saturn equatorial radius probed during each occultation as a function of inertial longitude, separately for RSS, VIMS, and UVIS. The early RSS occultations were a series of ansa-to-ansa diametric events that were sensitive to the absolute radius scale of the rings while relatively insensitive to Saturn's pole direction. VIMS and UVIS observed more partial or chord occultations that individually had joint sensitivity to the radius scale, pole direction, and ring inclination. A complementary view is provided by Fig. 2, which shows the ring opening angle $\sin B$ vs. inertial longitude sampled by the occultations. Here, the Earth-bound view of the Saturn system provided by the RSS experiments is restricted to $|B| \lesssim 25^\circ$ (or $|\sin B| \lesssim 0.4$). VIMS and UVIS occultations, on the other hand, sample more pole-on views that are less sensitive to ring inclinations and also less affected by small spacecraft trajectory errors, which are magnified for nearly edge-on views of the rings.

3.1. RSS

The *Cassini* Radio Science Subsystem (RSS) is capable of transmitting simultaneously at three wavelengths (λ =0.9, 3.6, and 13 cm), corresponding to the Ka, X, and S bands, respectively (Kliore et al., 2004). For this study, we restrict our attention to the X band observations, which typically have the highest SNR, although under favorable conditions the diffraction-corrected Ka band profiles have the highest spatial resolution. All of the RSS profiles used here were uniformly normalized and processed to remove the effects of diffraction using an optimized Fresnel filter, with a resulting spatial resolution of 1 km and a sample spacing of 0.25 km. In all, we make use of 34 separate ingress or egress RSS observations, listed in Table 1, from *Cassini* revs 7–125 (2005 May 3 – 2010 Jan 26); we omitted the rev 28 RSS occultation from our study because it was a very distant event with a poorly constrained spacecraft ephemeris, resulting in large uncertainties in the event geometry.[2] The event label is encoded as `RSS_rrrd_wnn`, where `rrr` is the rev number, `d` is the direction of the event (`I` for ingress and `E` for egress), `w` is the band, and `nn` refers to the receiving ground station, whose full identifier is `DSS-nn`.

In an analogous fashion to the influence of the finite star diameter on the 28 Sgr observations described previously, the 1 km effective resolution of the diffraction reconstruction resulted in small but systematic biases (relative to the higher resolution UVIS and

[2] *Cassini* diffraction-corrected RSS profiles for revs 7–67 are available from NASA's Planetary Data System Ring-Moon Systems Node (https://pds.jpl.nasa.gov/).

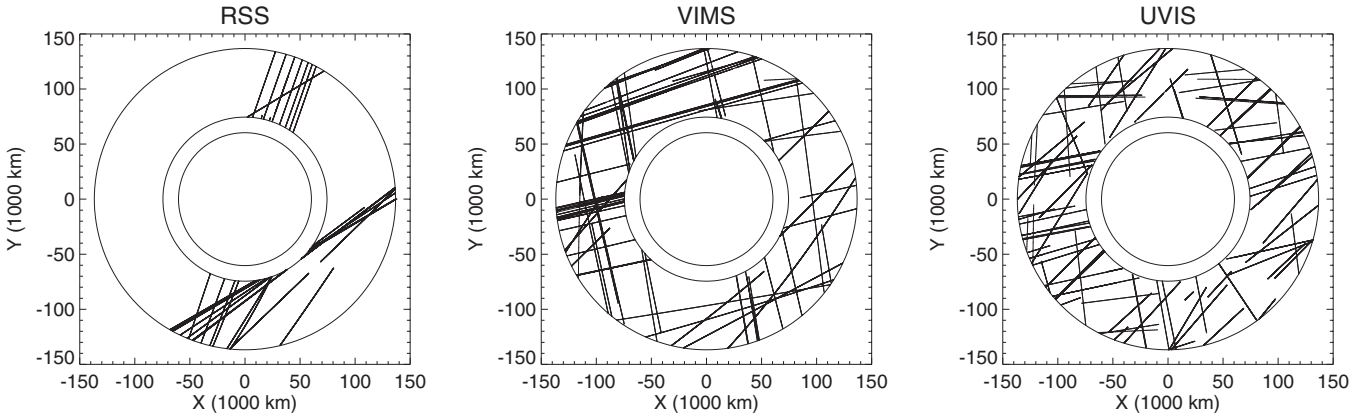

Fig. 1. Polar projection of occultation tracks in Saturn's equatorial plane for *Cassini* RSS, VIMS, UVIS, in inertial coordinates. From inner to outer, the circles correspond to Saturn, the inner edge of the C ring, and the outer edge of the A ring. The dense band of VIMS tracks near 180° longitude corresponds to a set of 17 occultations of γ Crucis observed in 2008/9.

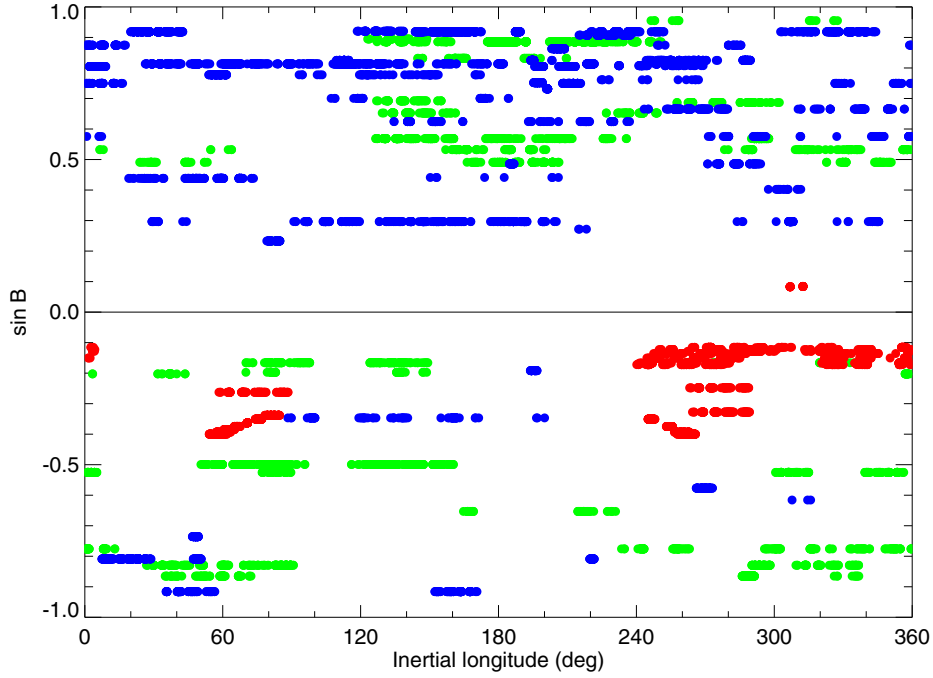

Fig. 2. Ring opening angle sin B as viewed from Earth (for RSS occultations), or from the spacecraft (for UVIS and VIMS occultations) vs inertial longitude of *Cassini* observations of individual ring features included in our adopted solution for the ring radius scale (red: RSS, green:VIMS, blue:UVIS). (For interpretation of the references to colour in this figure legend, the reader is referred to the web version of this article.)

VIMS results) in the fitted radii of a number of ring features whose intrinsic optical depth profiles were somewhat gradual and asymmetric. When this systematic bias exceeded 0.1 km for a given ring, we included a constant radial offset to the RSS observations of that ring as an additional free parameter in the least squares orbit fit, which effectively removed the bias at the expense of the addition of a degree of freedom for that ring. Since most rings had of order 100 or more measurements, this was a very small penalty to pay for a greatly improved fit.[3]

3.2. VIMS

The *Cassini* Visual and Infrared Mapping Spectrometer (VIMS) instrument has a highly capable occultation observing mode (Brown et al., 2004), in which the IR channel records a series of 0.5–5.1 μm spectra from a single pixel targeted at a star, with typical sampling intervals of 20–80 ms (Hedman et al., 2010). We use data exclusively from the spectral channel at 2.9 μm, where very strong absorption by water ice renders the background signal from the rings almost negligible. Since the VIMS instrument is mounted to the spacecraft itself, rather than to the originally planned but ultimately eliminated *Cassini* scan platform, the pointing during a typical occultation is remarkably steady, and in most instances the stellar image remains nearly fixed relative to the target pixel, resulting in excellent photometric stability. In all, we have made use of 95 separate ingress or egress VIMS occultation chords for this study (Table 1), from revs 13–197 (2005 Aug 20 – 2013 Sept 10). Events are listed alphabetically, using the code `VIMS_sssnnnd`, where `sss` is the variable-length abbreviated star identifier, `nnn` is the rev number, and `d` is the direction of the event (`I` for ingress and `E` for egress). For chord occultations, we treat the ingress and egress portions as separate events. VIMS occultations include reg-

[3] These radial offsets are included in the ring orbit fits tabulated in the SM.

ular data gaps during which the background signal is measured, and we excluded individual VIMS ring features in cases where a data gap affected the fitted ring edge location.

3.3. UVIS

The *Cassini* Ultraviolet Imaging Spectrograph (UVIS) includes a High Speed Photometer (HSP) designed for stellar occultations, with a sampling interval of 2–8 ms and a wavelength range of 110–190 nm (Esposito et al., 2004; Colwell et al., 2006). Over most of this spectral range water ice has a very low albedo, rendering the ring background negligible. We have used 107 separate ingress or egress UVIS occultation chords for this study (Table 1), from revs 7–194 (2005 May 21 – 2013 July 8). Events are listed alphabetically, using the code `UVIS_sssnnnd`, where `sss` is the variable-length abbreviated star identifier, `nnn` is the rev number, and `d` is the direction of the event (`I` for ingress and `E` for egress).

4. Occultation geometry

4.1. Overview

Our geometric framework for the Saturn ring system is an inertial reference frame centered at the solar system barycenter. To incorporate occultation observations, we implement the vector calculation developed in detail in Appendix A.1 of F93, including topocentric, Saturn barycenter, and non-relativistic light travel time corrections, as well as the effects of general relativistic bending of starlight by Saturn to order J_2. As described in F10, we make extensive use of the ICY interface to NASA's NAIF SPICE toolkit (Acton 1996), which provides a library of useful routines for translating between reference frames, as well as easy access to standard planetary ephemerides and spacecraft trajectory files. We use the J2000 heliocentric reference frame, the IAU 1976 model for the Earth shape (Abalakin, 1981), and the ITRF93 Earth rotation model (Boucher et al., 1994). In a minor revision to the F93 algorithm, we account for general relativistic bending by Saturn for Earth-based stellar occultations only, solving for the deflection at the time the occultation ray is closest to Saturn in the sky plane, rather than at the time at which the occultation ray penetrates the ring plane, as implied by Eqs. (A20)–(A23) of F93. Finally, we make use of Earth observatory positions as tabulated by JPL's Horizons website (Giorgini et al., 1996), and DSN coordinates as provided by JPL.

Our orbit fitting code, dubbed RINGFIT, is implemented in the IDL language, a commercial programming language available from Harris Geospatial Solutions. We have made extensive tests of our fitting program, primarily with a completely independent code developed by one of us (RAJ) , comparing both intermediate calculations and the final results of ring orbit fits. The two fitting codes use quite different least-squares fitting algorithms, and RINGFIT uses finite differences to compute partial derivatives, whereas the RAJ code uses analytic derivatives. In detailed tests, our calculated ring plane radii for Earth-based and spacecraft stellar occultations, as well as RSS events, agree to better than 1 m, and our fitted orbital elements for ring features and our derived Saturn pole direction agree to a very small fraction of the formal uncertainties of our least-squares fits. All formal errors and correlation coefficients for our fitted parameters are virtually identical.

4.2. Spacecraft and planetary ephemerides

For this study, we require spacecraft ephemerides for the *Voyager* Saturn encounters, the two *HST* stellar occultations, and the *Cassini* stellar and RSS occultations, and ideally a single planetary ephemeris to provide the state vectors of the Earth and Saturn relative to the solar system barycenter over the full course

Table 2
Kernel files.[a]

File
sat286.bsp
vgr1.sat286.bsp
vgr2.sat286.bsp
HST1081HSPephemUTC.bsp[b]
HST5824FOSephemUTC.bsp[b]
070918AP_SCPSE_07261_10191.bsp
080520AP_SCPSE_08138_10182.bsp
050606R_SCPSE_05114_05132.bsp
050623R_SCPSE_05132_05150.bsp
050708R_SCPSE_05150_05169.bsp
050802R_SCPSE_05169_05186.bsp
050825R_SCPSE_05186_05205.bsp
050907R_SCPSE_05205_05225.bsp
050922R_SCPSE_05225_05245.bsp
051011R_SCPSE_05245_05257.bsp
051021R_SCPSE_05257_05275.bsp
051114R_SCPSE_05275_05293.bsp
051213R_SCPSE_05293_05320.bsp
060111R_SCPSE_05320_05348.bsp
060213R_SCPSE_05348_06005.bsp
060321R_SCPSE_06005_06036.bsp
060417R_SCPSE_06036_06068.bsp
060515R_SCPSE_06068_06099.bsp
060614R_SCPSE_06099_06130.bsp
060719R_SCPSE_06130_06162.bsp
060810R_SCPSE_06162_06193.bsp
060907R_SCPSE_06193_06217.bsp
060925R_SCPSE_06217_06240.bsp
061013R_SCPSE_06240_06260.bsp
061108R_SCPSE_06260_06276.bsp
061116R_SCPSE_06276_06292.bsp
061129R_SCPSE_06292_06307.bsp
061213R_SCPSE_06308_06318.bsp
070109R_SCPSE_06318_06332.bsp
070117R_SCPSE_06332_06342.bsp
070125R_SCPSE_06342_06356.bsp
070208R_SCPSE_06356_07008.bsp
070213R_SCPSE_07008_07023.bsp
070312R_SCPSE_07023_07042.bsp
070405R_SCPSE_07042_07062.bsp
070430R_SCPSE_07062_07077.bsp
070507R_SCPSE_07077_07094.bsp
070517R_SCPSE_07094_07106.bsp
070605R_SCPSE_07106_07125.bsp
070625R_SCPSE_07125_07140.bsp
070705R_SCPSE_07140_07155.bsp
070727R_SCPSE_07155_07170.bsp
070822R_SCPSE_07170_07191.bsp
071017R_SCPSE_07191_07221.bsp
071127R_SCPSE_07221_07262.bsp
080117R_SCPSE_07262_07309.bsp
080123R_SCPSE_07309_07329.bsp
080225R_SCPSE_07329_07345.bsp
080307R_SCPSE_07345_07365.bsp
080327R_SCPSE_07365_08045.bsp
080428R_SCPSE_08045_08067.bsp
080515R_SCPSE_08067_08078.bsp
080605R_SCPSE_08078_08126.bsp
080618R_SCPSE_08126_08141.bsp
080819R_SCPSE_08141_08206.bsp
080916R_SCPSE_08206_08220.bsp
081031R_SCPSE_08220_08272.bsp
081126R_SCPSE_08272_08294.bsp
081217R_SCPSE_08294_08319.bsp
090120R_SCPSE_08319_08334.bsp
090202R_SCPSE_08334_08350.bsp
090225R_SCPSE_08350_09028.bsp
090423R_SCPSE_09028_09075.bsp
090507R_SCPSE_09075_09089.bsp
090520R_SCPSE_09089_09104.bsp

(*continued on next page*)

Table 2 (*continued*)

File
090609R_SCPSE_09104_09120.bsp
090624R_SCPSE_09120_09136.bsp
090701R_SCPSE_09136_09153.bsp
090708R_SCPSE_09153_09168.bsp
090806R_SCPSE_09168_09184.bsp
090817R_SCPSE_09184_09200.bsp
090921R_SCPSE_09200_09215.bsp
090924R_SCPSE_09215_09231.bsp
091116R_SCPSE_09231_09275.bsp
091208R_SCPSE_09275_09296.bsp
100107R_SCPSE_09296_09317.bsp
100113R_SCPSE_09317_09339.bsp
100114R_SCPSE_09339_09355.bsp
100127R_SCPSE_09355_10003.bsp
100209R_SCPSE_10003_10021.bsp
100325R_SCPSE_10021_10055.bsp
100420R_SCPSE_10055_10085.bsp
100519R_SCPSE_10085_10110.bsp
100616R_SCPSE_10110_10132.bsp
100625R_SCPSE_10132_10146.bsp
100706R_SCPSE_10146_10164.bsp
100726R_SCPSE_10164_10178.bsp
100913R_SCPSE_10178_10216.bsp
101013R_SCPSE_10216_10256.bsp
101210R_SCPSE_10256_10302.bsp
101215R_SCPSE_10302_10326.bsp
110204R_SCPSE_10344_11003.bsp
110224R_SCPSE_10326_10344.bsp
110308R_SCPSE_11003_11041.bsp
110504R_SCPSE_11041_11093.bsp
110519R_SCPSE_11093_11119.bsp
110721R_SCPSE_11119_11150.bsp
111010R_SCPSE_11150_11246.bsp
111014R_SCPSE_11246_11267.bsp
111123R_SCPSE_11267_11303.bsp
120117R_SCPSE_11303_11337.bsp
120119R_SCPSE_11337_11357.bsp
120227R_SCPSE_11357_12016.bsp
120312R_SCPSE_12016_12042.bsp
120416R_SCPSE_12042_12077.bsp
120426R_SCPSE_12077_12098.bsp
120523R_SCPSE_12098_12116.bsp
120628R_SCPSE_12116_12136.bsp
120820R_SCPSE_12136_12151.bsp
120829R_SCPSE_12151_12199.bsp
121130R_SCPSE_12199_12257.bsp
121204R_SCPSE_12257_12304.bsp
130318R_SCPSE_12304_12328.bsp
130319R_SCPSE_12328_13038.bsp
130321R_SCPSE_13038_13063.bsp
130417R_SCPSE_13063_13087.bsp
130710R_SCPSE_13087_13137.bsp
130805R_SCPSE_13137_13182.bsp
130807R_SCPSE_13182_13200.bsp
131024R_SCPSE_13200_13241.bsp
131105R_SCPSE_13241_13273.bsp
131212R_SCPSE_13273_13314.bsp
earthstns_itrf93_040916.bsp
earth_070425_370426_predict.bpc
earth_720101_070426.bpc
cpck22Jan2015.tpc[c]
naif0011.tls

[a] Available from http://naif.jpl.nasa.gov/pub/naif/

[b] Constructed from archive data obtained from the Space Telescope Science Institute for the two *HST* occultations; provided in the online Supplementary Material (SM)

[c] Note that the Saturn pole direction is explicitly determined by the least-squares fit, and not taken from this planetary constants file.

of the observations. (As part of this work, we apply empirical corrections to some of the nominal spacecraft trajectories, as described in Section 5.1 below.) Table 2 lists the ephemerides and other important constants files (known as kernel files) used for the orbit fits. As is customary for use with NAIF software, the kernels are listed in increasing order of precedence: successive files overrule previous files when they cover the same time domain and geometric situation. This order is important, since in practice there are slight differences between the underlying planetary ephemerides used for the individual spacecraft kernel files. The *Voyager* encounters are based on the DE-286 planetary ephemeris, the *HST* ephemerides (obtained from the Space Telescope Science Institute's online data archives) give geocentric state vectors in the J2000 system, and *Cassini* kernels (with names such as 130318R_SCPSE_12304_12328.bsp) are reconstructed trajectory files provided by the *Cassini* Navigation Team based on the best planetary ephemeris and Saturn pole direction known at the time. We discuss below possible consequences of this mixture of underlying planetary ephemerides and assumed pole directions for our results.

Table 2 also includes files that define the locations of the DSN stations, the rotation state of the Earth, a planetary constants file, and a leap-seconds file (required to convert between the TDT and UTC, since data are recorded in UTC and trajectories are in TDT). Note that we do not make use of the Saturn pole direction given in the planetary constants file, but solve for it as part of our global solution for the Saturn ring system geometry.

4.3. Occultation stars

The occultation star positions used in this study are given in Table 3. For the *Cassini* stellar occultations, we use *Hipparcos* catalog positions when available, and we apply parallax (at Saturn) and proper motion corrections as calculated individually for each ring event time. In principle, our orbit fitting software can solve for corrections to the catalog positions as part of the overall geometric solution for the full set of occultation data, but in practice we have found that such fitted corrections are unrealistically large and are strongly correlated with corrections for spacecraft trajectories. Therefore, for the *Voyager* and *Cassini* occultations, we accept the catalog star positions as known quantities, and absorb any slight errors in the positions into our low-order corrections to the spacecraft ephemerides. For the Earth-based 28 Sgr and *HST* occultations, we solve instead for offsets to the a priori positions of the stars, without correcting for the Earth or *HST* ephemerides. The effect of an error in the stellar position $\delta\theta$ is to introduce an error $D\delta\theta$ into the derived location of the feature in the ring plane, where D is the distance of the observer from the rings. For *Cassini* occultations $D \lesssim 10^6$ km, whereas for Earth-based occultations $D \simeq 10^9$ km. Typically, $\delta\theta \sim 10$ mas $\sim 10^{-7}$ rad. For all historical (pre-*Cassini*) stellar occultations, we adopt the a priori star coordinates given in Table 1 of F10 for consistency with previous results; these are also included in Table 3 for convenient reference.

4.4. Saturn's pole

Saturn's pole undergoes forced precession due primarily to the solar torque on Saturn's equatorial satellites (Ward, 1975). As described more recently by F93, the Sun exerts a torque on Saturn's oblate figure, as well as on the orbits of the equatorial satellites. The relatively weak Sun-satellite torques in turn act on Saturn through the much stronger planet-satellite torques due to Saturn's oblateness, with massive Titan making the dominant contribution to the overall precession, followed by Iapetus. The associated pole precession period is then proportional to the sum of the angular

Table 3
A priori star positions.

Star	Catalog ID[a]	α(°)[b]	$\sigma(\alpha)$ (mas)	δ(°)[b]	$\sigma(\delta)$ (mas)	π (mas)	μ_{α^*} (mas yr^{-1})	μ_δ (mas yr^{-1})
2Cen	67457	207.36146360	0.62	−34.45063035	0.49	18.39 ± 0.74	−42.59 ± 0.88	−59.87 ± 0.64
AlpAra	85792	262.96050660	0.88	−49.87598159	0.44	13.46 ± 0.95	−31.27 ± 0.89	−67.15 ± 0.44
AlpAur	24608	79.17206517	0.80	45.99902927	0.51	77.29 ± 0.89	75.52 ± 0.77	−427.13 ± 0.50
AlpCMa	32349	101.28854110	1.21	−16.71314306	1.04	379.21 ± 1.58	−546.01 ± 1.33	−1223.08 ± 1.24
AlpLup	71860	220.48239100	0.46	−47.38814127	0.45	5.95 ± 0.76	−21.15 ± 0.54	−24.22 ± 0.62
AlpLyr	91262	279.23410830	0.48	38.78299311	0.47	128.93 ± 0.55	201.02 ± 0.57	287.46 ± 0.60
AlpOri	27989	88.79287161	1.51	7.40703634	1.13	7.63 ± 1.64	27.33 ± 2.30	10.86 ± 1.46
AlpSco	80763	247.35194800	1.52	−26.43194608	1.08	5.40 ± 1.68	−10.16 ± 2.00	−23.21 ± 1.34
AlpVir	65474	201.29835230	0.75	−11.16124491	0.54	12.44 ± 0.86	−42.50 ± 0.79	−31.73 ± 0.52
BetCen	68702	210.95601900	0.43	−60.37297840	0.44	6.21 ± 0.56	−33.96 ± 0.51	−25.06 ± 0.45
BetCru	62434	191.93049540	0.42	−59.68873246	0.40	9.25 ± 0.61	−48.24 ± 0.49	−12.82 ± 0.50
BetGru	112122	340.66639530	0.58	−46.88456594	0.49	19.17 ± 0.75	135.68 ± 0.64	−4.51 ± 0.53
BetLib	74785	229.25196590	0.75	−9.38286694	0.52	20.38 ± 0.87	−96.39 ± 0.89	−20.76 ± 0.68
BetLup	73273	224.63314190	0.55	−43.13386699	0.40	6.23 ± 0.71	−34.06 ± 0.82	−38.30 ± 0.62
BetPeg	113881	345.94305580	0.46	28.08245462	0.46	16.37 ± 0.72	187.76 ± 0.52	137.61 ± 0.56
BetPer	14576	47.04220716	0.71	40.95565120	0.58	35.14 ± 0.90	2.39 ± 0.77	−1.44 ± 0.88
CWLeo[c]	9475740	146.98919000	0.11	13.27877000	0.19	0.00 ± 0.00	0.00 ± 0.00	0.00 ± 0.00
DelCen	59196	182.08976510	0.50	−50.72240999	0.55	8.25 ± 0.79	−47.53 ± 1.14	−6.42 ± 1.11
DelLup	75141	230.34306830	0.79	−40.64745946	0.61	6.39 ± 0.86	−19.11 ± 0.88	−24.05 ± 0.72
DelPer	17358	55.73117540	1.45	47.78765330	1.00	6.18 ± 0.85	23.83 ± 0.68	−41.93 ± 0.71
EpsCMa	33579	104.65644450	0.37	−28.97208931	0.42	7.57 ± 0.57	2.63 ± 0.48	2.29 ± 0.57
EpsCen	66657	204.97196960	0.40	−53.46636269	0.55	8.68 ± 0.77	−14.60 ± 0.55	−12.79 ± 0.83
EpsLup	75264	230.67036470	0.93	−44.68957314	0.73	6.47 ± 0.61	−20.25 ± 0.83	−20.13 ± 0.71
EpsMus	59929	184.39431800	0.36	−67.96067161	0.38	10.80 ± 0.48	−231.26 ± 0.36	−26.37 ± 0.40
EpsPsA	111954	340.16385650	0.94	−27.04361480	0.50	4.38 ± 0.87	22.01 ± 1.51	−0.88 ± 0.79
EtaLup	78384	240.03058540	0.64	−38.39664079	0.49	6.61 ± 0.78	−16.58 ± 0.69	−27.06 ± 0.64
GamAra	85267	261.34858270	0.60	−56.37768824	0.52	2.87 ± 0.75	−0.77 ± 0.72	−15.85 ± 0.59
GamCas	4427	14.17708808	0.35	60.71674966	0.38	5.32 ± 0.56	25.65 ± 0.42	−3.82 ± 0.44
GamCru	61084	187.79137200	0.39	−57.11256922	0.42	37.09 ± 0.67	27.94 ± 0.54	−264.33 ± 0.47
GamGru	108085	328.48189200	0.65	−37.36482290	0.45	16.07 ± 0.77	95.88 ± 0.76	−12.10 ± 0.47
GamPeg	1067	3.30895828	0.67	15.18361593	0.44	9.79 ± 0.81	4.70 ± 0.77	−8.24 ± 0.56
KapCen	73334	224.79041250	0.60	−42.10414199	0.46	6.05 ± 0.73	−17.76 ± 0.56	−21.33 ± 0.61
KapVel	45941	140.52845510	0.39	−55.01069531	0.42	6.05 ± 0.48	−10.72 ± 0.45	11.24 ± 0.45
LamSco	85927	263.40219370	0.74	−37.10374835	0.52	4.64 ± 0.90	−8.90 ± 0.92	−29.95 ± 0.58
LamVel	44816	136.99907130	0.41	−43.43262406	0.40	5.69 ± 0.53	−23.21 ± 0.50	14.28 ± 0.41
MuCen	67472	207.40419930	0.54	−42.47368506	0.42	6.19 ± 0.71	−23.85 ± 0.62	−19.22 ± 0.42
MuCep	107259	325.87689560	0.45	58.78005308	0.43	0.62 ± 0.52	5.24 ± 0.48	−2.88 ± 0.49
Pi4Ori	22549	72.80152507	0.71	5.60510146	0.52	2.59 ± 0.80	−3.62 ± 0.97	1.03 ± 0.63
RCar	46806	143.06103170	0.72	−62.78892185	0.88	7.84 ± 0.83	−36.22 ± 0.76	19.70 ± 1.10
RCas	118188	359.60330660	0.98	51.38876254	1.09	9.37 ± 1.10	84.39 ± 0.95	18.07 ± 0.88
RDor	21479	69.19032350	0.67	−62.07698129	0.61	16.02 ± 0.69	−68.46 ± 0.73	−71.22 ± 0.78
RHya	65835	202.42841190	1.41	−23.28135784	0.94	1.62 ± 2.43	−60.73 ± 1.68	11.01 ± 1.19
RLeo	48036	146.88954480	1.27	11.42889439	0.68	9.87 ± 2.07	−0.57 ± 1.48	−42.70 ± 0.68
RLyr	92862	283.83368820	0.45	43.94589260	0.47	9.33 ± 0.52	19.94 ± 0.49	80.60 ± 0.64
RSCnc	45058	137.66168930	0.88	30.96321920	0.59	8.21 ± 0.98	−9.41 ± 1.08	−33.05 ± 0.50
SigSgr	92855	283.81631960	0.87	−26.29659428	0.45	14.54 ± 0.88	13.87 ± 1.09	−52.65 ± 0.60
TheCar	52419	160.73927800	0.45	−64.39447937	0.45	7.43 ± 0.50	−18.87 ± 0.85	12.06 ± 0.90
WHya	67419	207.25846060	0.91	−28.36749079	0.66	8.73 ± 1.09	−49.05 ± 1.13	−59.58 ± 0.84
ZetCMa	30122	95.07827982	0.40	−30.06337656	0.43	9.70 ± 0.58	8.00 ± 0.54	3.81 ± 0.51
ZetCen	68002	208.88514540	0.57	−47.28826634	0.43	8.48 ± 0.74	−57.14 ± 0.52	−44.75 ± 0.42
ZetPer	18246	58.53299363	0.63	31.88365776	0.45	3.32 ± 0.75	4.41 ± 0.88	−9.15 ± 0.69
ZetPup	39429	120.89612560	0.41	−40.00318846	0.40	2.33 ± 0.51	−30.82 ± 0.44	16.77 ± 0.41
δ Sco[d]		240.08339900		−22.62162600				
28 Sgr[e]		281.58576800		−22.39218600				
	GSC 5249-01240[f]	349.89416040		−6.786242694				
	GSC 6323-01396[g]	302.62652910		−20.61319170				

[a] Hipparcos catalog (Agency, 1997), unless otherwise noted
[b] Epoch JD 2448349.0625 = JD1991.25 (TT) for Hipparcos positions; J2000 otherwise
[c] 2Mass catalog (Skrutskie et al., 2006)
[d] Adopted a priori position for *Voyager 2* stellar occultation (French et al., 2010)
[e] Adopted a priori position for 1989 July 3, stellar occultation (French et al., 2010)
[f] Adopted a priori position (French et al., 2010) for HST program 5824 occultation star from the Hubble guide star photometric catalog (Bucciarelli et al., 2001)
[g] Adopted a priori position (French et al., 2010) for HST program 1081 occultation star from the Hubble guide star photometric catalog (Bucciarelli et al., 2001)

momentum of Saturn's rotation and the orbital motion of its equatorial satellites, divided by the solar torque exerted on the satellites and Saturn's oblate figure. F93 estimate a theoretical long-term average of the precession period of

$$P = 1.5603 \times 10^6 (\cos\epsilon)^{-1} \mathrm{yr}, \quad (1)$$

where ϵ is the obliquity of Saturn's spin axis with respect to the invariable plane. For $\epsilon = 27.34^\circ$, $P = 1.7565 \times 10^6$ yr. The corresponding angular rate of polar motion is

$$\dot{\Omega}_P \equiv 360^\circ/P = 0.0205^\circ \mathrm{cy}^{-1} = 0.74'' \mathrm{yr}^{-1}, \quad (2)$$

Table 4
Saturn geometry fits.

Fit #	Data Sets		Pole Solution					
	Cassini 28 Sgr	*Voyager HST*	$\alpha_P(^\circ)$[a] $\delta_P(^\circ)$[a]	$\dot{\alpha}_P(^\circ\ \mathrm{cy}^{-1})$[a] $\dot{\delta}_P(^\circ\ \mathrm{cy}^{-1})$[a]	PA(°) $\dot{\hat{n}}_P(''\ \mathrm{yr}^{-1})$	$\dot{\Omega}_P(''\mathrm{yr}^{-1})$ $\sigma(\dot{\hat{n}}_P)/\dot{\hat{n}}_P$	N rms (km)	Notes Fit ID
1	X		40.579414 ± 0.000062	−0.03497 ± 0.00405	129.47 ± 4.54	0.400 ± 0.041	8239	C, B, CD circular features, unweighted
			83.537218 ± 0.000009	−0.00324 ± 0.00048	0.184 ± 0.019	0.103	0.134	Sa025S-RF-V5574
2	X		40.579803 ± 0.000089	−0.04444 ± 0.00615	125.95 ± 5.52	0.484 ± 0.052	8239	Fit #1, but no trajectory corr. or RSS bias
			83.537196 ± 0.000009	−0.00363 ± 0.00055	0.222 ± 0.024	0.106	1.122	Sa025S-RF-V5578
3	X		40.579410 ± 0.000051	−0.03210 ± 0.00363	130.77 ± 4.08	0.374 ± 0.037	8239	Fit #1, but weighted by ring
			83.537227 ± 0.000008	−0.00311 ± 0.00042	0.172 ± 0.017	0.099	0.135	Sa025S-RF-V5574wtd
4	X		40.579395 ± 0.000045	−0.02477 ± 0.00321	142.96 ± 3.61	0.363 ± 0.031	15260	All rings, weighted by ring
			83.537201 ± 0.000007	−0.00370 ± 0.00033	0.167 ± 0.014	0.085	0.477	Sa025S-RF-V5978
5	X	X	40.579422 ± 0.000044	−0.02940 ± 0.00275	144.30 ± 2.96	0.445 ± 0.016	15304	All rings, weighted by ring and observation
			83.537202 ± 0.000007	−0.00461 ± 0.00017	0.204 ± 0.007	0.035	0.477	Sa025S-RF-V5979
6	X	X	40.579423 ± 0.000044	−0.02977 ± 0.00257	143.93 ± 2.68	0.446 ± 0.014	15469	All rings, weighted by ring and observation
	X		83.537202 ± 0.000007	−0.00460 ± 0.00017	0.205 ± 0.007	0.032	0.498	Sa025S-RF-V5980
7	X	X	40.579425 ± 0.000044	−0.03062 ± 0.00248	143.24 ± 2.55	0.451 ± 0.014	15683	All rings, weighted by ring and observation
	X	X	83.537202 ± 0.000007	−0.00461 ± 0.00017	0.207 ± 0.006	0.030	0.540	Sa025S-RF-V5981

[a] The epoch is UTC 2008 Jan 1, 12:00:00

while the motion of Saturn's pole *on the sky* is given by

$$\dot{\hat{n}}_P = \dot{\Omega}_P \sin\epsilon = 0.0094^\circ \mathrm{cy}^{-1} = 0.34'' \mathrm{yr}^{-1}, \quad (3)$$

where $\dot{\hat{n}}_P$ is the time derivative of the unit vector in the direction of Saturn's pole. Over time spans comparable to the nodal regression periods (Vienne and Duriez, 1992; 1995) of Titan (∼ 700 yrs) and Iapetus (∼ 3200 yrs), however, oscillations in the instantaneous precession rate of ± 50% are expected (Nicholson et al., 1999). Furthermore, as we discuss below, nutation of Saturn's other major satellites (Vienne and Duriez, 1992) may also contribute to variations in the direction and rate of Saturn's precession on time scales as short as a few years to a few decades, although a complete theory for polar precession that incorporates these terms has not yet been developed.

Uncertainties in this estimate, in decreasing order of importance, stem primarily from uncertainties in Saturn's moment of inertia, its interior rotation period, the approximate treatment of the Iapetus torque, and the exclusion of shorter period contributions associated with Saturn's other equatorial satellites. For this study, we have implemented several physically-based models developed by one of us (RAJ) for the detailed motion of Saturn's pole over the ∼ 33 yr span of our occultation observations, but we find that none of them provides a statistically significant improvement in our best fitting precession results over a simple linear approximation to the pole precession rate and direction. Given the uncertainties in the pole direction implicit in the current best set of reconstructed *Cassini* spacecraft ephemerides, and the planned improved and self-consistent solution for the *Cassini* trajectory by the *Cassini* Navigation Team upon the conclusion of the orbital tour in 2017, we defer until later a detailed investigation of Saturn's pole precession, and instead adopt a linear model for the polar motion in this work. As we will show, in spite of these open questions, our fitted pole precession rate is in excellent agreement with independent estimates derived from ring plane crossing (RPX) times and with theoretical predictions based on Titan's nutation (Vienne and Duriez, 1992). Furthermore, we demonstrate that our derived absolute radius scale is quite tightly constrained and largely independent of the assumed pole precession model.

5. Ring orbit fits

5.1. Overall approach

The RINGFIT orbit fitting code implements an algorithm that solves for the set of ring orbital elements that minimize the (possibly weighted) sum of squared residuals between the observed and model ring plane radii, using a standard kinematical model for all ring features. We refer the reader to Paper 2 Section 4 and Appendix A), which contains a detailed description of our underlying model of an inclined, precessing keplerian ellipse, with allowance for additional free or forced modes of radial distortion of wavenumber m, amplitude A_m, and pattern speed Ω_p. The least-squares fit also incorporates additional fittable physical and geometrical parameters, including the direction and precession rate of Saturn's pole, offsets to the catalog positions of Earth-based occultation stars, time offsets for individual 28 Sgr light curves (see F93 and F10), systematic radial offsets for selected rings for 28 Sgr and RSS observations as discussed above, and corrections for the nominal spacecraft trajectories (see below). Our most general fit includes 980 free parameters fitted to 15683 data points for 122 ring features. All of our fits have a common epoch for the ring orbital elements of 2008 Jan 1, 12:00 UTC (JD 245 4467.0).

As noted in Paper 2, an essential part of our solution is to derive corrections to the spacecraft trajectory for each stellar or radio occultation chord, since the typical *a priori* uncertainty in the *Cassini* spacecraft location is ∼ 1 km, which in the case of grazing viewing geometries can be amplified in the derived ring plane radius. Our simplest correction is a one-parameter along-track timing offset Δt for each relevant segment of the spacecraft trajectory spanning a given ingress or egress occultation chord. This pre-

serves the dynamical shape of the trajectory, and simply shifts it in time; in most cases, the largest *a priori* uncertainty in the spacecraft's location is in this along-track direction, justifying this approach. This single parameter also acts to correct for any small errors in the catalog position of the occulted star, although as we have noted above, it is not possible to separate these two contributions to the fitted value of Δt for a given occultation.

In some cases, this simple one-parameter correction is not sufficient to compensate for systematic trends in the radial residuals along a given occultation chord, and in those instances we included an additional fitted parameter to subtract this slope. Combining these two correction factors, the corrected model ring plane radius $r_{\rm corr}(t)$ at time t is given by

$$r_{\rm corr}(t) = r(t + \Delta t) - \alpha(r - r_0)/1000, \quad (4)$$

where $r(t + \Delta t) = r(t) + \dot{r}\Delta t$, $r(t)$ is the uncorrected radius at time t, $\dot{r}(t)$ is the ring plane radial velocity at time t, we set the constant $r_0 = 100{,}000$ km, and α is the fitted non-dimensional slope parameter (in units of km per 1000 km). For $\alpha \simeq 0.01$ (a typical value from Table 1) and $r - r_0 = 10^4$ km, the corresponding correction $r_{\rm corr} - r \simeq 0.1$ km. We note that fitting for Δt for all occultations (and α for selected events) does not destroy our sensitivity to the absolute radius scale because of the very large number of occultations we use.

Our principal goal for this work is to establish an absolute radius scale for the rings. Ideally, this means that in any given occultation data set, there is an accurate mapping between the observed time on the light curve and the ring plane radius sampled by that particular occultation ray. In practice, while we generally have a continuous recording across part of the ring system, there is a limited number of sharp-edged fiducial features that can be used to register the time domain onto a radial scale. In previous work based on historical occultations, Simpson et al. (1983), Nicholson et al. (1990), F93, and Bosh et al. (2002) identified a set of putatively circular features to serve as markers, and solved for the radii of these features as part of their general solution for the Saturn ring system geometry. F93 identified 30 such features as part of their preferred solution (see their Table X), with an additional more poorly constrained set of eight features in the B ring. For each ring feature, the number of fitted data points ranged from 5 to 19.

We adopted a similar approach in our studies of the B ring edge (Paper 1), C ring (Paper 2), and Cassini Division (Paper 3), restricting our attention to *Cassini* data. As described in Paper 3, we iteratively identified a set of putative circular and equatorial ring features, and after each iteration removed candidate rings that were measurably eccentric or inclined, or had unacceptably large rms errors. In the end, this yielded $\sim$ 60 circular features in the C ring, B ring, and Cassini Division, for a total of over 6000 data points; no well-fitted or nearly circular features were found in the A ring, which was not the target of those investigations. For our Cassini Division study, individual nominally circular features had from 83 to 142 measurements, with rms residuals in all cases less than $\sigma = 0.25$ km, and in some cases below 0.10 km.

This provided an extremely accurate local radius scale that enabled detection of a host of weak normal modes on ringlet and gap edges, some with radial amplitudes below 0.10 km. However, it does not meet our present need to extend the radius scale to include the A ring, and by its nature it excluded a large number of well-fitted but non-circular sharp-edged ringlets and gaps that could contribute to the accuracy and extent of the derived radius scale. The restriction to quasi-circular features in the pre-*Cassini* studies was justifiable because of the relatively small number of data points per ring; fitting an elliptical ring model would have added three additional free parameters to the fit for each ring. By expanding our included data set to include non-circular rings, and by appropriately weighting the data to account for the varied quality of individual ring fits and of different occultation events, we take advantage of the full set of available observations without suppressing the influence of the best-fitting rings. Furthermore, by including several features in the outer A ring, we greatly expand the set of occultation events that can be registered on an accurate radius scale.

5.2. Atlas of fitted ring features

Fig. 3 shows a radial optical depth profile of the rings from an early RSS diametric occultation, with optical depth increasing downwards to provide a direct comparison with a similar figure in F93 (Fig. 4). Our adopted radius scale is based on measurements of the 122 ring features identified by vertical tick marks (95 of which are effectively circular, as we discuss below). The top panel shows the inner C ring, with an abundance of sharp features less than 78,000 km in radius, followed by a hiatus where the broad undulations in the middle C ring are largely devoid of sharp features, with the notable exception a 40 km wide ringlet at 79,240 km (the inner and outer edges correspond to F93 features 38 and 37, respectively). Moving to the plateau region of the outer C ring in the second panel, we again find a host of sharp features. The B ring is largely devoid of identifiable sharp ring features with well-fitting keplerian orbits except in the B2 region between 99 000 and 104,000 km. The Cassini Division, in the next-to-last panel, hosts 22 sharp-edged ringlets and gaps. Finally, the A ring has virtually no sharp-edged features, and of these only three have reasonably stable orbits: the inner and outer edges of the Encke Division near 133,500 km and the outer edge of the Keeler Gap near 136,400 km. The outer edge of the A ring is strongly perturbed over time by the mutual orbital exchange of Janus and Epimetheus (El Moutamid and coauthors, 2016), and we exclude this feature from our present study. Note that many of the presumed "circular" features from previous studies (Nicholson et al., 1990; French et al., 1993) are now known to have small forced perturbations due to the Titan 1:0 and Mimas 2:1 resonances (see Fig. 19 of Paper 2 and Fig. 25 of Paper 3, respectively).

6. Radius scale and pole direction

6.1. Overview

In this section, we present a series of fits for the geometry of the Saturn ring system, beginning with a restricted set of very high quality *Cassini* data, and then successively incorporating additional observations, including historical data from *Voyager*, 28 Sgr, and *HST* occultations. As part of the solution, we solve for Saturn's pole direction and linear precession rate, which we compare to previous determinations, and we quantify the sensitivity of the derived absolute radius scale to the geometry of the pole. Using our preferred solution, we compare the present absolute radius scale with that of F93.

6.2. Fits to Saturn's pole and ring radius scale

The radius scale upon which we based our Paper 3 study of features in the Cassini Division was derived from an unweighted fit of *Cassini* RSS, UVIS, and VIMS occultation measurements for the orbital elements of 67 quasi-circular features in the C and B rings and Cassini Division, spacecraft ephemeris corrections for 194 separate ingress or egress occultation tracks, and Saturn's pole direction and linear precession rate. Fit #1 in Table 4 is identical to the Paper 3 solution except for the elimination of six duplicate data points that had been inadvertently included in the Paper 3 fit.

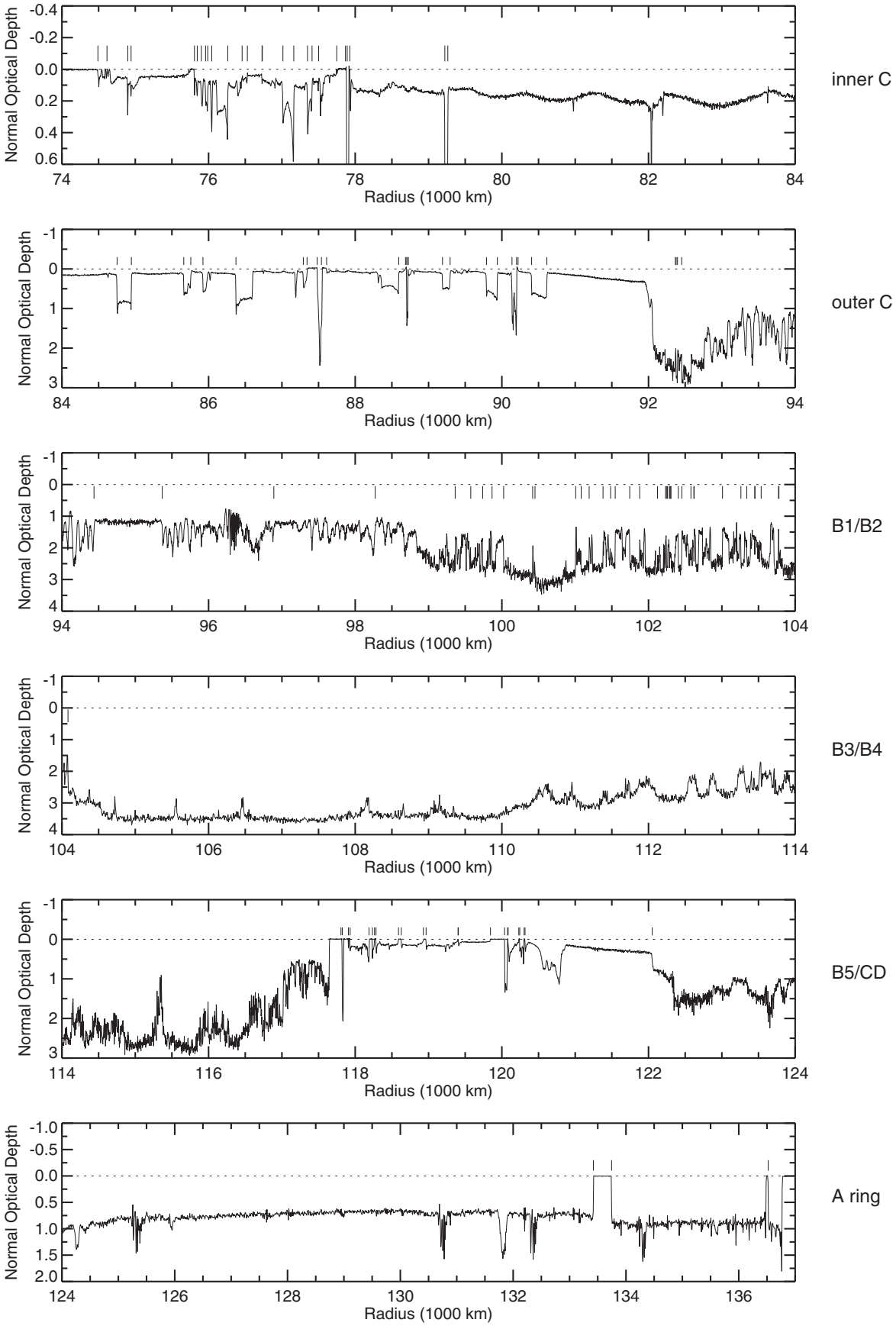

Fig. 3. Radial optical depth profile of Saturn's rings (from event RSS_007E_X43, Table 1), showing the 122 ring features fitted in this work. Each ring region is labeled at right.

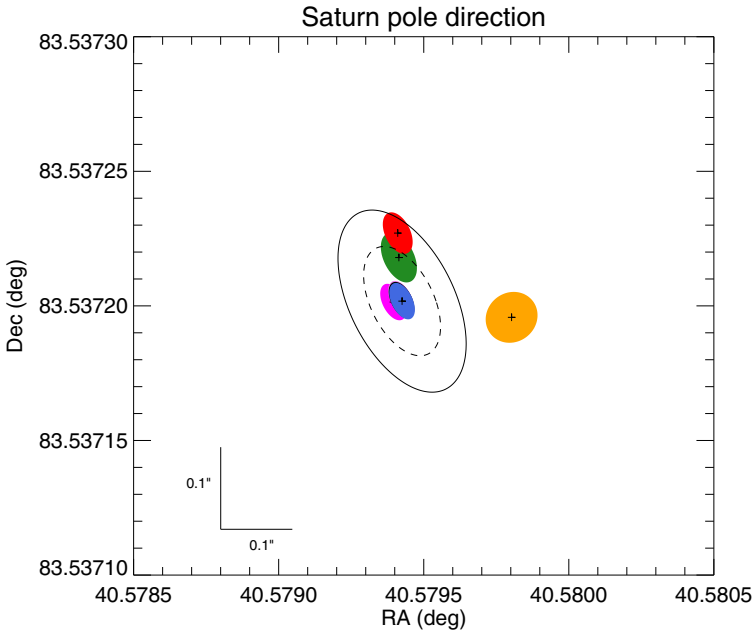

Fig. 4. Saturn pole direction in J2000 coordinates at the J2008 epoch. The error ellipses overlap sequentially in numerical order of the fits in Table 4, with the color scheme as follows: Fits #1–#4 (*Cassini* only): green, orange (recall that this fit did not account for trajectory errors or RSS radial biases), red, and magenta; Fit #5 (*Voyager* added): violet (barely visible behind best fit); Fit #6 (28 Sgr added): black (barely visible behind best fit); and Fit #7 (*HST* added): blue. The dashed and solid concentric error ellipses correspond to 3- and 5-σ formal errors from Fit #7. For context, see the overview plot in Fig. 9. (For interpretation of the references to colour in this figure legend, the reader is referred to the web version of this article.)

Here, as for all of the model fits, we have assumed a simple linear precession model for the pole direction at time t:

$$\alpha_P(t) = \alpha_P + (t - t_0)\dot{\alpha}_P \tag{5}$$

and

$$\delta_P(t) = \delta_P + (t - t_0)\dot{\delta}_P, \tag{6}$$

where α_P and δ_P are the pole direction (in degrees) at epoch t_0, $(t - t_0)$ is the epoch-relative time in Julian centuries, and $\dot{\alpha}_P$ and $\dot{\delta}_P$ are the precession rates (in deg cy^{-1}) in right ascension and declination, respectively. We also include the fitted pole precession rate in polar coordinates, where *PA* is the position angle in degrees, measured counterclockwise from North, and $\dot{\hat{n}}_P$ is the linear precession rate in arcsec per yr on the sky (see Eq. (3)). We included along-track trajectory errors for the *Cassini* spacecraft for all ingress or egress arcs, as given in Eq. (4). We included the slope parameter α when its inclusion materially improved the fit and its fitted value was at least twice its formal uncertainty. All of the rings were modeled as circular and equatorial, with the following exceptions: Cassini Division features 9, 13, 15, and 118 (see Table 5, Paper 3 for the correspondence between feature name and feature ID) were fitted as precessing ellipses, and features 9, 13, and 15 additionally included the forced $m = 2$ normal mode induced by Mimas; in the inner C ring, we included the distortion due to the Titan $m = 1$ resonance when it was measurable (see Fig. 19, Paper 2). The post-fit rms radius residual for Fit #1 is just 0.134 km for the 8239 fitted points. Fig. 4 shows the fitted pole direction and the 1-σ error ellipse at our J2008 epoch for this and subsequent fits.

Fit #1 includes correction terms for the *Cassini* reconstructed trajectories, as well as compensation for the biases in some ring measurements resulting from the finite resolution of the RSS occultation profiles, as described previously. Fit #2 illustrates the effect of ignoring both of these effects: the rms residual jumps to 1.122 km (an increase of over a factor of 8 from Fit #1), and the pole direction and precession rate change by several standard deviations, confirming the importance of including these correction terms.

In Fit #1, the ring-by-ring rms residuals varied by over a factor of two, from 0.081 km for the best-fitting ring to 0.211 km for the worst-fitting ring in this particular solution. These residuals include contributions from measurement errors as well as intrinsic deviations in the orbital shape from the assumed orbital model. To account for this variability from ring to ring, we performed a weighted fit (Fit #3), in which we iteratively assigned a weight of $1/\sigma_i^2$ to all data points for a given ring i, where σ_i is the rms residual for the ith ring from the previous iteration; only a few iterations were required for convergence of the weighting scheme. The results are quite consistent with Fit #1, with a slight reduction in the formal uncertainty in the pole direction and precession rates.

In all of the fits described so far, we restricted the data sets to quasi-circular, equatorial features, but as shown in Paper 2 and Paper 3, there are numerous ringlet and gap edges with manifestly non-circular shapes, including some with statistically significant inclinations. Some of these features have quite robust fits, with small rms errors – for example, the Maxwell ringlet OER (outer edge of the ringlet) post-fit residuals are only 0.16 km (Table 2, Paper 2). Therefore, in a similar spirit to Fit #3, we expanded the *Cassini* data set for Fit #4 to include all ringlet edges and gaps with post-fit residuals below 1.50 km, amounting in the end to 15260 data points for 122 ring features, including A ring features 1, 3, and 4 (respectively, the Keeler gap OEG (outer edge of the gap) and the outer and inner Encke gap edges (OEG and IEG)); the inner edge of the Keeler Gap and the outer edge of the A ring itself have significant unmodeled perturbations in excess of 1.50 km (El Moutamid and coauthors, 2016; Tajeddine et al., 2017) and were excluded from the fit. These fit results are also shown in Table 4, where most notably the formal errors in the pole direction and precession rate are further reduced from Fit #3, and the fractional error in the fitted pole precession rate is now under 10%.

With *Cassini* data alone, the 8.5% uncertainty from Fit #4 in the precession rate exceeds by over a factor of four the *a priori*

uncertainty in Saturn's moment of inertia of about 2% based on planetary interior models (W. Hubbard, personal communication), and thus does not contribute meaningfully to our knowledge of the planet's interior. Ultimately, we would like to make use of the more than 30-year span of the combined historical and *Cassini* data sets to tighten the constraint on the pole precession rate. To this end, we performed a series of fits in which we successively added earlier occultation observations. In Fit #5, we added the *Voyager 1* and *2* data described in F93 to the *Cassini* data in Fit #4. As free parameters, we included along-track time corrections for the *Voyager* spacecraft ephemerides, but not the α term for either *Voyager* encounter. For this fit, we implemented a hybrid iterative weighting scheme in which all of the *Voyager* (*1* or *2*) data were weighted as $1/\sigma_{Vgr}^2$, where σ_{Vgr} is the *a posteriori* rms residual of the ensemble of *Voyager* (*1* or *2*) data from the previous iteration, and the *Cassini* data were weighted ring-by-ring by $1/\sigma_i^2$, as before, but where σ_i is the now rms residual for the *i*'th ring for the *Cassini* data only. There were 44 additional data points from the *Voyager* set, with $\sigma_{Vgr} = 0.508$ km for the 20 points from *Voyager 1* and 0.707 km for the 24 points from *Voyager 2*. The fitted ephemeris offset times for the *Voyager* trajectories were 0.033 ± 0.008 s and -0.008 ± 0.015 s, respectively. The results of Fit #5 are also shown in Table 4 and Fig. 4. The most notable improvement from the *Cassini*-only fit is the reduction in the formal fractional error of the pole precession rate from 0.085 to 0.035, but with a concomitant more than 2-σ increase in its *value* compared to Fit #4. We will return to this point when we compare the derived precession rates from the full set of fits.

Next, in Fit #6, we added the substantial set of observations of the 3 July 1989 28 Sgr occultation, fitting for corrections to the occulted star position and offset times for selected Earth-based stations as in F93 analysis. We weighted the 302 data points from the 28 Sgr event as an ensemble with an *a posteriori* value of $\sigma_{28\ Sgr} = 1.146$ km (and $\sigma_{Vgr} = 0.505$ km and 0.711 km for the two *Voyager* encounters, respectively; very similar to the Fit #5 case). Overall, Fit #6 differs very little from Fit #5; the *Voyager* data are the dominant contributor to the tightened constraint on the pole precession rate, owing both to the extended time baseline of the observations and the sensitivity of the fit to the nearly edge-on geometry of the *Voyager* RSS observations.

Finally, in Fit #7, we included the *HST* occultation data sets described in F10, weighting the aggregates of the two individual occultations separately, as for the other historical occultations. As noted previously, the fitted midtimes of the ring events have rather large uncertainties, reflected in the *a posteriori* values $\sigma_{HST} = 2.747$ km for the 48 data points of the 1991 occultation, and $\sigma_{HST} = 3.380$ km for the 29 data points of 1995 event. This fit to 122 ring features includes a total of 15683 individual ring measurements, 980 free parameters, and with unweighted rms radius residuals of 0.540 km. The fractional error in the pole precession rate is just 3%. This is our adopted solution, representing our most comprehensive solution for Saturn's pole direction and radius scale.

Table 5 lists the fitted radii of the 67 nominally circular features in Fit #1 (note that orbit models for rings 9, 13, 15, and 118 also include keplerian ellipses, contributing up to 0.25 km to the local radii of these features, as discussed previously and in Paper 3) and the 28 additional nominally circular features included among the 122 circular and non-circular features included in Fit #7.[4] For most users, these $67 + 28 = 95$ features will be adequate to serve as fiducials for our adopted radius scale; users willing to go to the extra effort of computing the time-dependent orbital radii for all 122 features are directed to the Appendix and the SM. The more limited reference radii from F93 are included as well, along with the differences between the F93 radii and our fitted values. We remind users that our complete fits also include the effects of the $m = 1$ normal mode forced by Titan, with contributions varying inversely as the distance from the Titan ringlet ($a = 77879$ km) in the C ring, and in excess of 0.25 km for features with radii between 76,725 and 78,000 km (see Paper 2). We also include the $m = 2$ mode forced by Mimas in the Cassini Division, contributing up to 0.5 km to the local radius in this region (see Paper 3). These features, as well as rings 9, 13, 15, and 118, are probably best excluded by users who require sub-km accuracy in the radius scale but do not wish to go to the effort of using the full orbital elements documented in the SM. See the Appendix for further guidance on the use of these results.

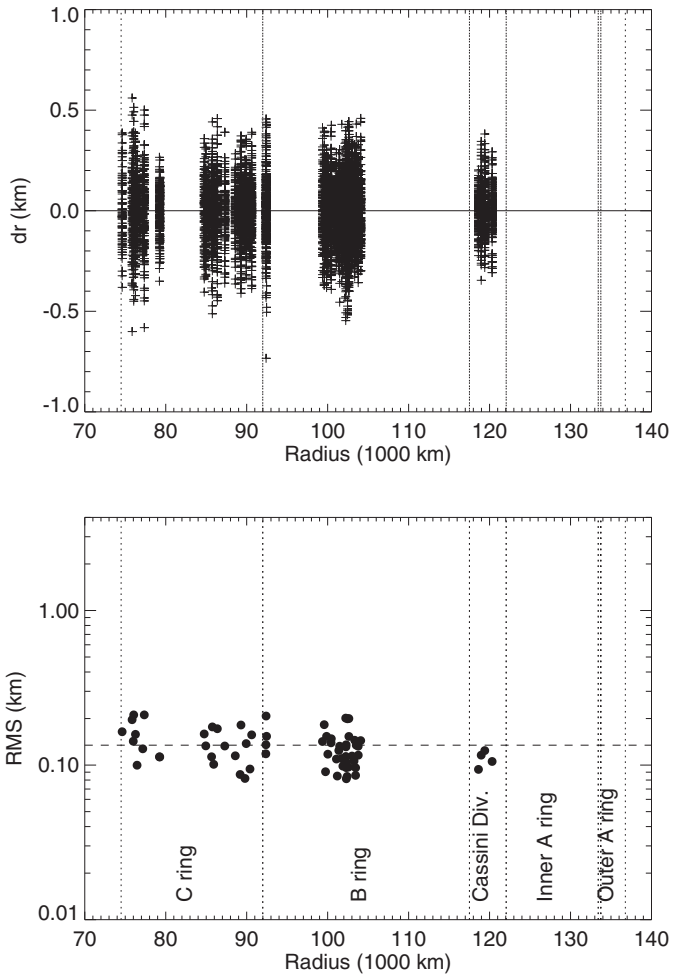

Fig. 5. Post-fit residuals and rms residuals for Fit #1, an unweighted fit to 67 quasi-circular features using *Cassini* data only. The overall rms of the fit of 0.134 km is shown as a horizontal dashed line. There are no notable outliers among these features.

6.3. Radius residuals

One measure of the quality of the geometric fits is the pattern of residuals with ring orbital radius. Fit #1 is our most restrictive solution, utilizing only very high quality *Cassini* observations of 67 quasi-circular features in the C and B rings, and the Cassini Division. Fig. 5 shows the individual and rms residuals as a function of radius for this unweighted fit. None of the 8239 data points has a radial residual greater than 0.8 km, and the vast majority under 0.4 km, testifying to the high quality of the data, the applicability

[4] The fitted orbital elements of all 122 features, both circular and non-circular, are included in the SM.

Table 5
Quasi-circular fiducial features for absolute radius scale.

ID	Feature type	F93 r(km)	Fit #1 r(km)	dr(km)[(d)]	Fit #7 r(km)	dr(km)[(d)]
44	IER	74490.760			74490.508 ± 0.036	0.252
135			74614.739 ± 0.025		74614.733 ± 0.022	
137					74898.625 ± 0.023	
138					74942.737 ± 0.020	
139					75806.774 ± 0.023	
140			75845.198 ± 0.028		75845.186 ± 0.032	
141					75901.173 ± 0.074	
143					75958.942 ± 0.062	
144			75988.658 ± 0.027		75988.649 ± 0.024	
145			76043.295 ± 0.026		76043.277 ± 0.030	
40	OER	76263.930	76261.773 ± 0.026	2.157	76261.774 ± 0.024	2.156
348			76457.675 ± 0.026		76457.661 ± 0.018	
149					76529.231 ± 0.032	
151[(a)]					76733.013 ± 0.037	
152[(a)]					77014.109 ± 0.034	
39[(a)]	OER	77164.830	77162.114 ± 0.026	2.716	77162.104 ± 0.022	2.726
153[(a)]			77349.119 ± 0.027		77349.110 ± 0.030	
154[(a)]					77411.053 ± 0.038	
155[(a)]					77501.350 ± 0.054	
487[(a)]					77747.848 ± 0.036	
43[(a)]					77925.940 ± 0.029	
38	IER	79220.310	79222.044 ± 0.026	−1.734	79222.028 ± 0.018	−1.718
37	OER	79265.280	79262.910 ± 0.026	2.370	79262.891 ± 0.019	2.389
35	IER	84749.440	84751.774 ± 0.025	−2.334	84751.760 ± 0.022	−2.320
34	OER	84949.380	84947.292 ± 0.025	2.088	84947.281 ± 0.020	2.099
33	IER	85660.650	85661.961 ± 0.025	−1.311	85661.952 ± 0.018	−1.302
42	OER	85758.590	85757.245 ± 0.025	1.345	85757.229 ± 0.024	1.361
31	IER	85921.380	85923.705 ± 0.026	−2.325	85923.694 ± 0.019	−2.314
30	IER	86370.610	86373.173 ± 0.025	−2.563	86373.166 ± 0.025	−2.556
162			87291.762 ± 0.025		87291.750 ± 0.020	
163					87342.681 ± 0.034	
28	OER	88594.290	88592.736 ± 0.025	1.554	88592.726 ± 0.019	1.564
111					88685.884 ± 0.118	
59					88701.783 ± 0.030	
58					88719.207 ± 0.038	
110					88722.995 ± 0.029	
27	IER	89188.600	89190.586 ± 0.025	−1.986	89190.571 ± 0.017	−1.971
41	OER	89295.060	89294.056 ± 0.025	1.004	89294.045 ± 0.022	1.015
26	IER	89786.800	89789.578 ± 0.025	−2.778	89789.560 ± 0.017	−2.760
25	OER	89939.280	89937.791 ± 0.025	1.489	89937.778 ± 0.020	1.502
24	IER	90404.080	90406.126 ± 0.025	−2.046	90406.114 ± 0.018	−2.034
23	OER	90614.870	90613.798 ± 0.025	1.072	90613.780 ± 0.022	1.090
176			92366.300 ± 0.026		92366.287 ± 0.020	
177			92376.712 ± 0.025		92376.694 ± 0.021	
178			92395.165 ± 0.026		92395.151 ± 0.028	
179			92452.821 ± 0.026		92452.803 ± 0.022	
83	IEG	94439.460			94437.544 ± 0.108	1.916
82	OEG	95365.200			95368.375 ± 0.149	−3.175
81	IEG	96895.970			96890.360 ± 0.152	5.610
78	OER	98278.490			98271.949 ± 0.214	6.541
272			99363.039 ± 0.025		99363.024 ± 0.021	
277			99576.113 ± 0.025		99576.093 ± 0.022	
280			99738.562 ± 0.025		99738.544 ± 0.018	
284			99865.921 ± 0.025		99865.901 ± 0.021	
77			100024.406 ± 0.025		100024.389 ± 0.019	
286			100420.178 ± 0.025		100420.160 ± 0.020	
287			100451.971 ± 0.025		100451.945 ± 0.020	
76	IEG	101002.530			101006.748 ± 0.038	−4.218
288			101081.943 ± 0.025		101081.926 ± 0.019	
289			101190.082 ± 0.025		101190.066 ± 0.017	
292			101379.300 ± 0.025		101379.283 ± 0.019	
293			101482.868 ± 0.025		101482.852 ± 0.020	
75	IEG	101543.480			101545.952 ± 0.047	−2.472
74			101743.408 ± 0.025		101743.390 ± 0.019	
296			101879.535 ± 0.025		101879.522 ± 0.018	
299			102122.394 ± 0.025		102122.379 ± 0.018	
302			102231.656 ± 0.026		102231.638 ± 0.025	
303			102245.529 ± 0.025		102245.516 ± 0.019	
304			102257.611 ± 0.025		102257.592 ± 0.019	
305			102283.107 ± 0.025		102283.092 ± 0.020	
306			102291.066 ± 0.025		102291.052 ± 0.018	
352			102303.001 ± 0.025		102302.987 ± 0.018	
353			102305.840 ± 0.025		102305.825 ± 0.017	

(*continued on next page*)

Table 5 (*continued*)

ID	Feature type	F93 r(km)	Fit #1 r(km)	dr(km)[(d)]	Fit #7 r(km)	dr(km)[(d)]
308			102405.687 ± 0.025		102405.674 ± 0.017	
309			102454.792 ± 0.025		102454.781 ± 0.024	
311			102578.805 ± 0.026		102578.793 ± 0.018	
313			102618.489 ± 0.025		102618.478 ± 0.024	
314			102622.171 ± 0.025		102622.160 ± 0.021	
73			103008.645 ± 0.025		103008.631 ± 0.019	
323			103260.338 ± 0.025		103260.323 ± 0.018	
325			103340.838 ± 0.025		103340.827 ± 0.020	
326			103448.485 ± 0.025		103448.469 ± 0.018	
328			103452.139 ± 0.025		103452.126 ± 0.018	
329			103536.207 ± 0.025		103536.195 ± 0.020	
331			103772.499 ± 0.025		103772.487 ± 0.019	
332			103778.783 ± 0.025		103778.771 ± 0.019	
71	OEG	104087.190	104082.651 ± 0.025	4.539	104082.645 ± 0.021	4.545
13[(b)]	OEG	118628.110	118628.397 ± 0.026	−0.287	118628.384 ± 0.018	−0.274
15[(b)]	OEG	118965.690	118966.703 ± 0.025	−1.013	118966.689 ± 0.019	−0.999
118[(b)]			119406.273 ± 0.027		119406.286 ± 0.020	
9[(b)]			120316.038 ± 0.026		120316.027 ± 0.018	
7	IER	122049.480			122050.077 ± 0.090	−0.597
4	IEG	133423.530			133423.239 ± 0.067	0.291
3	OEG	133745.140			133744.838 ± 0.062	0.302
1[(c)]	OEG	136522.280			136522.088 ± 0.088	0.192

[(a)] These features are affected by the forced $m = 1$ Titan mode with amplitude greater than 0.25 km – see Section 6.2
[(b)] Fitted as keplerian ellipse with forced $m = 2$ Mimas mode – see Section 6.2
[(c)] Fitted as keplerian ellipse with $ae = 0.99$ km – see Table 6 of SM
[(d)] The difference between the F93 radius and our fitted value, for each fit.

of simple keplerian orbit models to these features, and the efficacy of the trajectory corrections in reducing the spacecraft position errors to a small fraction of the typical *a priori* value of 1 km. The lower panel shows the rms errors, which tend to decrease slightly with orbital radius from the C ring to the Cassini Division.

In comparison, Fig. 6 shows the individual and unweighted rms residuals for Fit #7, our adopted joint solution for the radius scale based on a weighted fit to 122 features from the full set of historical observations. The larger individual residuals compared to Fit #1 result from a combination of larger feature measurement uncertainties in the pre-*Cassini* data and the inclusion of ring features with larger intrinsic scatter, some of which probably results from unmodeled orbital perturbations. Nevertheless, the unweighted rms residuals are for the most part well below 1 km, a substantial improvement over the F93 results (see Fig. 13 of F93 for a comparison). Note that the lower overall residuals in the B2 region are an artifact of including only *Cassini* data for most of these features, since they were usually too difficult to measure in the other data sets.

6.4. Comparison of Fit #7 with F93 radius scale

The differences between the fitted radii from our adopted Fit #7 and the *Cassini* -only Fit #1 using a restricted set of very high quality data are very small, as shown in Fig. 7 and listed in Table 5. The systematic difference in the radius scale between the two fits is an insignificant 0.013 km, confirming that the inclusion of the historical data sets does not materially change the derived radius scale. We now compare the results of our adopted solution with the F93 results for the absolute radius scale of the rings. As a reminder, F93 fitted a total of 397 data points from the *Voyager 1* and *2* occultations and the 28 Sgr event, with an rms residual of 1.295 km; our adopted solution includes 15,683 data points from the two *Voyager* occultations, the 28 Sgr event, the two *HST* occultations, and 236 *Cassini* RSS, VIMS, and UVIS occultation chords.

In Fig. 8 we plot *dr*, the difference between the F93 fitted orbital radii and our adopted Fit #7, as a function of orbital radius for 38 features regarded by F93 as quasi-circular. Filled symbols correspond to ringlet outer edges and gap inner edges (OER/IEG);

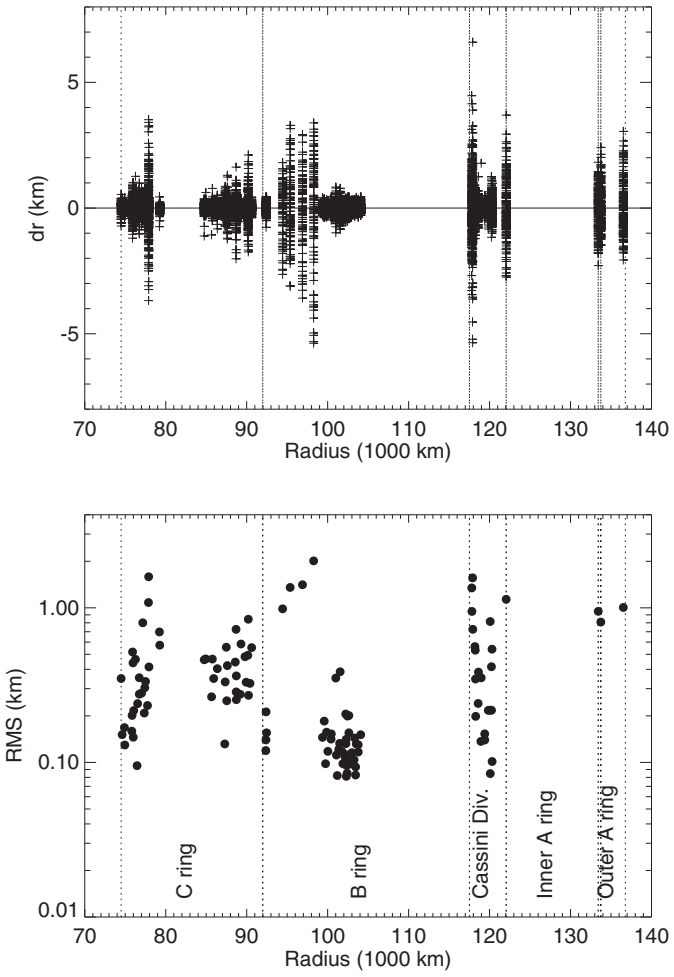

Fig. 6. Post-fit residuals of all 122 fitted rings to all data sets in Fit #7, our adopted solution.

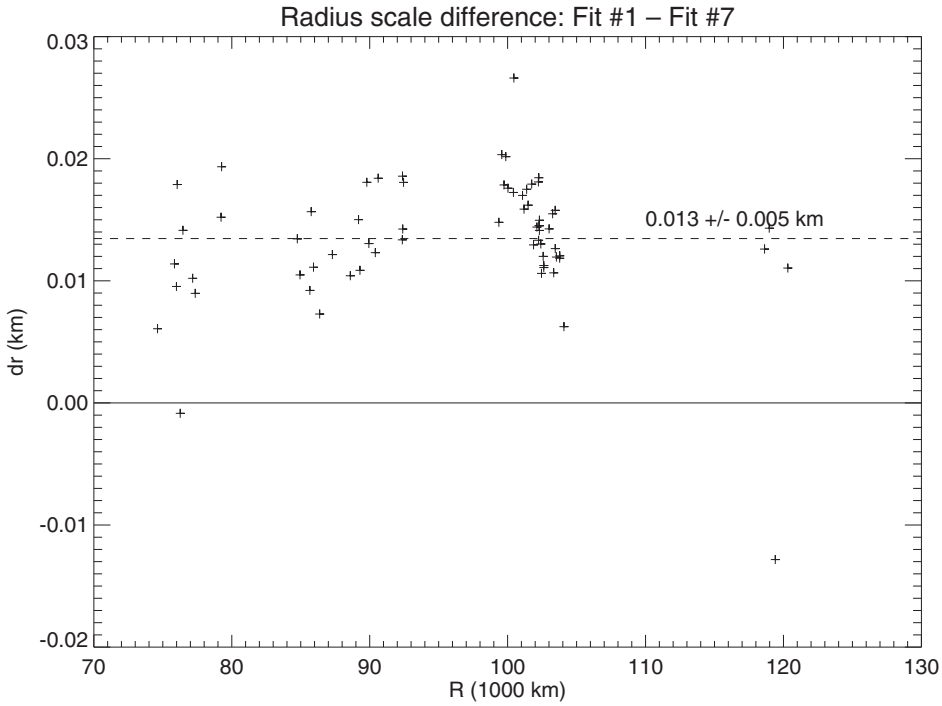

Fig. 7. Comparison of fitted radii of ring features in common between Fit #1 and Fit #7 (Table 5). On average, the Fit #1 radii are just 0.013 km greater than the Fit #7 radii, with an even smaller internal scatter of 0.005 km.

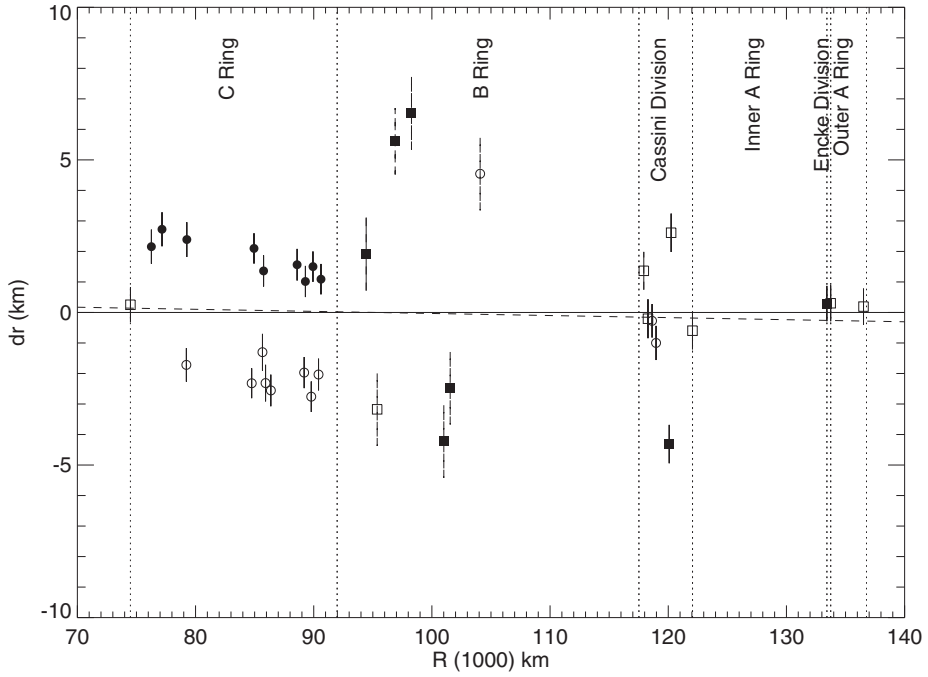

Fig. 8. Comparison of F93 ring feature radii and the results of Fit #7 of Table 4, where *dr* is the difference between the F93 solution and the Fit #7 value for the mean radius. Filled symbols correspond to outer edges of ringlets and inner edges of gaps (OER/IEG); open symbols correspond to inner edges of ringlets and outer edges of gaps (IER/OEG). Features (included in/excluded from) Fit #1 are plotted as (circles/squares). The error bars are the uncertainties in the fitted radii given by F93, which in every case are much larger than the uncertainties from Fit #7. Overall, the F93 radius scale agrees remarkably well with our adopted solution: the dashed line shows a weighted linear fit to *dr*. See text for details.

open symbols correspond to ringlet inner edges and gap outer edges (IER/OEG). Features that were included in the adopted fit but excluded from the more restrictive Fit #1 that utilized only very high SNR *Cassini* observations are plotted as squares. The F93 IER/OEG radii for ringlet *inner* edges and gap outer edges are typically smaller than our adopted solution by about 2 km in the C ring, while the reverse is true for ringlet *outer* edges and gap inner edges. F93 noted a similar systematic inward (outward) shift in the fitted radii for IERs (OERs) relative to the *Voyager* observations, for C ring plateau features (see F93, Figs. 11 and 12), attributable to the effects of substantial smoothing of the 28 Sgr observations by the $\sim$ 18 km projected diameter of the occulted star.

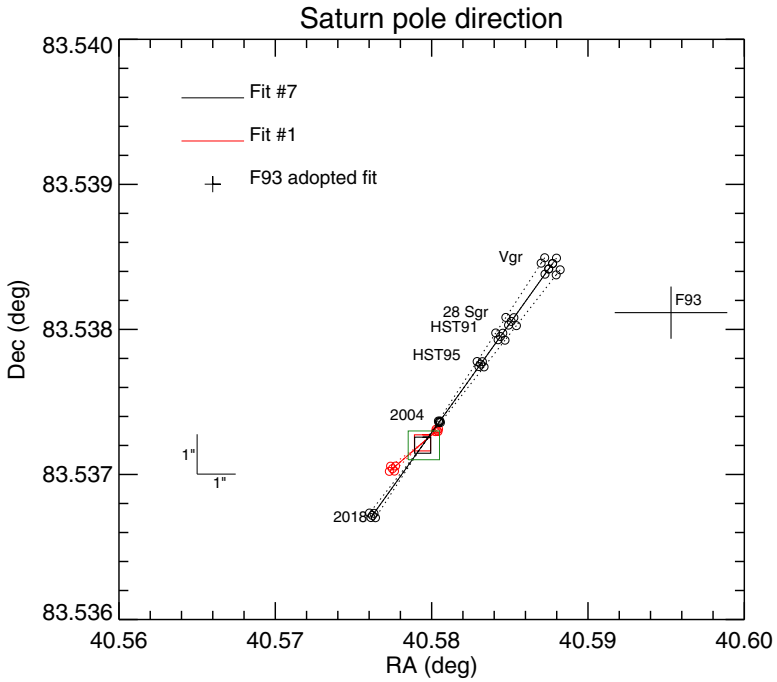

Fig. 9. Saturn pole direction and precession in the plane of the sky, from a variety of fits. The black lines and open circles show the results from Fit #7 (Table 4), our adopted fit to all available occultation data. The solid black line shows the precession path based on the fitted linear precession model; the dashed lines show the 1-σ uncertainties in the pole precession rate and direction, with the open circles showing the pole position at the individual epochs marked: Vgr for *Voyager 1* and *2*, 28 Sgr for the 3 July 1989 occultation, HST91 and HST95 for the 1991 and 1995 *HST* occultations, and 2004 to 2018 spanning the interval of the *Cassini* orbital tour. The pole direction at the J2008 epoch is marked as a black square. The corresponding results for Fit #1, based on a smaller set of *Cassini* -only data, are shown in red, plotted over the time interval of the data used in the fit. For comparison, we also show the F93 pole solution at the 1980 November 12 23:46:32 epoch (near the time of the *Voyager 1* flyby), which is significantly displaced from our current solution. The green square demarcates the region of the plot that is magnified in Fig. 4. (For interpretation of the references to colour in this figure legend, the reader is referred to the web version of this article.)

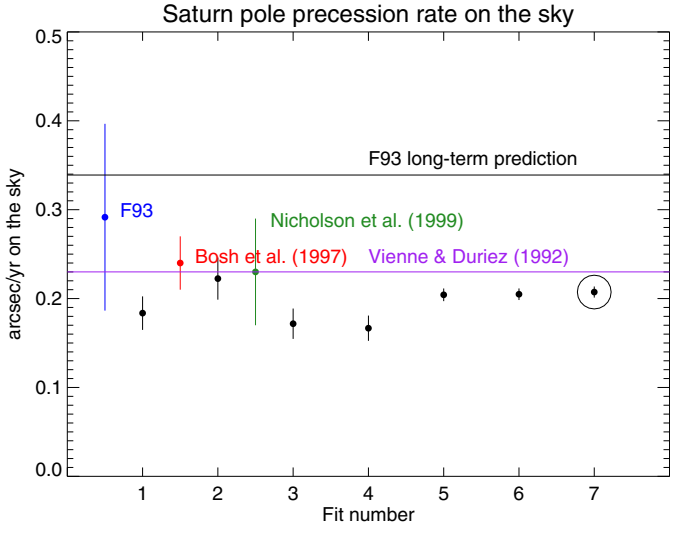

Fig. 10. Saturn pole precession rate on the sky $\dot{n}_P$ for each of the fits in Table 4, shown as black circles with formal error bars. Our favored solution, Fit #7, is encircled: $\dot{n}_P = 0.207 \pm 0.006''\text{yr}^{-1}$ (equivalent to $\Omega_P = 0.451 \pm 0.014''\text{yr}^{-1}$). Also shown are the F93 long-term prediction (ignoring Titan's nutation), the F93 result (blue) from the analysis of *Voyager* and 28 Sgr occultation data, the Bosh et al. (1997) result $\dot{n}_P = 0.24 \pm 0.03''\text{yr}^{-1}$ (red) from a combination of *Voyager* and Saturn RPX measurements, the independent estimate of $\dot{n}_P = 0.23 \pm 0.06''\text{yr}^{-1}$ from an analysis of over two centuries of Earth-based observations of RPX times (Nicholson et al., 1999), shown in green, and the theoretical estimate of $\dot{n}_P = 0.23''\text{yr}^{-1}$ (equivalent to $\Omega_P = 0.50''\text{yr}^{-1}$) by Vienne and Duriez (1992) based on a model of Titan's precession. (For interpretation of the references to colour in this figure legend, the reader is referred to the web version of this article.)

Despite these differences, on average the F93 radius scale agrees remarkably well with our adopted solution, which is likely due to the favorable ansa-to-ansa geometry of the 28 Sgr data, resulting in good estimates of the absolute radii of the rings. The dashed line in Fig. 8 shows a weighted linear fit to dr:

$$dr(r) = -0.033 - 0.00681 \times (r - 100,000)/1000 \text{ km}, \quad (7)$$

where r is measured in km. Note that $dr(r)$ should be *subtracted* from the radii of features registered on the F93 radius scale in order to place them on our adopted radius scale from Fit #7. In practice, this represents a very small systematic correction across the ring system: for r =70,000 km, $dr \simeq 0.17$ km and for r =140,000 km, $dr \simeq -0.31$ km. Nevertheless, users should be mindful of the much larger errors (on the scale of 1–2 km) that could result from using only OER/IEG (or IER/OEG) features from the F93 list to calibrate their observations. It is recommended that an equal mix of inner and outer edges be used, where possible.

6.5. Saturn pole direction and precession rate

We next compare our results for the direction and precession rate of Saturn's pole with previous results, summarized in Fig. 9. Our adopted solution from Fit #7 is shown in black – the black square marks the fitted pole direction at the J2008 epoch, and the diagonal solid black line shows the track of the pole direction over the course of time given by the fitted linear precession model. Small black circles denote the pole position at various epochs, with the earliest at the upper right (marking *Voyager 1* and *2*), followed by 28 Sgr, then the two *HST* occultations, and finally the interval from 2004 to 2018, corresponding to the entire span of the *Cassini* orbital tour of Saturn. The sensitivity of the pole direction and precession path to the formal errors in the fit is illustrated by the dashed lines, representing four fits in which the position angle of

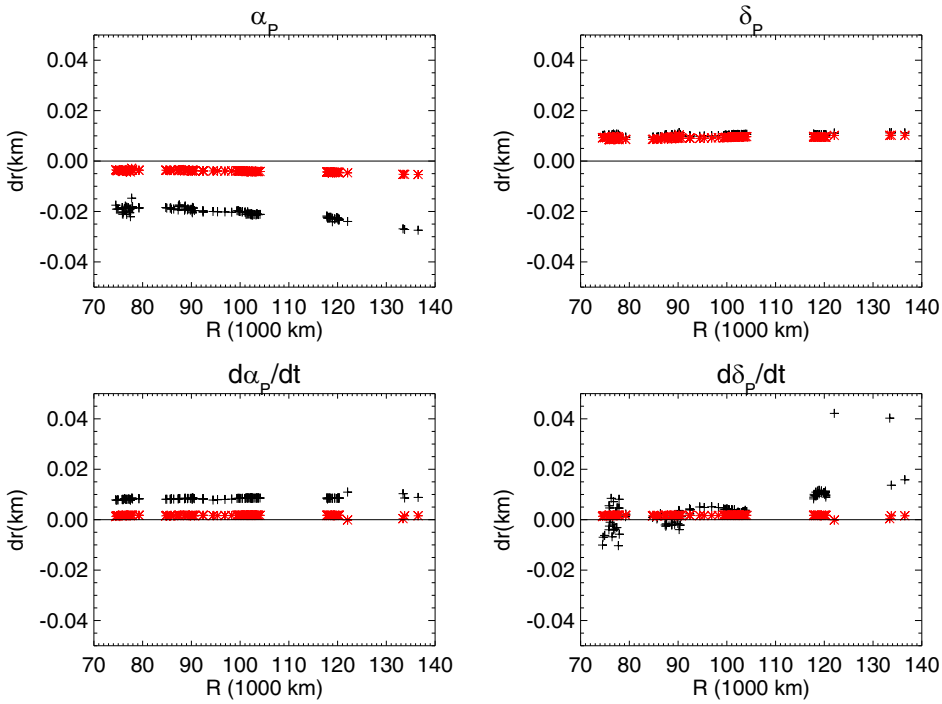

Fig. 11. Sensitivity of fitted ring radii to uncertainties in Saturn's pole direction and precession rate. The black ' + ' symbols show the changes in the fitted semimajor axes resulting from rerunning Fit #7 (Table 4), except for a fixed $1-\sigma$ increase in the pole parameter identified at the top of each panel; all other parameters in the fit were allowed to adjust to this constraint. The red symbols show the changes in radius calculated from the correlation matrix of Fit #7, under the assumption that all other parameters in the fit were unchanged. The top row shows the results for the pole direction at epoch, and the bottom row shows the results from changes in the precession rates in RA and Dec. The changes in radius from the constrained fits are generally quite small – of order a few tens of meters, in most cases – and the correlation matrix results give systematic changes of order 10 m or less. (For interpretation of the references to colour in this figure legend, the reader is referred to the web version of this article.)

the pole *PA* and then the precession rate $\dot{\hat{n}}_P$ were individually incremented by $\pm 1 - \sigma$ of the fitted values. The small circles illustrate the effect of these changes at the individually labeled epochs.

The red curves and open circles in Fig. 9 correspond to Fit #1, based on a shorter span of data since only *Cassini* observations were used in the fit. The red circles are located at the earliest and latest times of the data included in the fit, and once again illustrate the effect of changing the position angle and precession rate of the pole by the formal error of the fit. The green square marks the region of the plot that is magnified in Fig. 4. For comparison, the F93 adopted pole solution and error bars are shown in black. (Note that the epoch of the F93 pole is 1980 November 12 23:46:32 UTC, compared to the J2008 epoch for our solutions.) If the F93 and Fit #7 pole solutions were identical, the F93 pole would lie along the black diagonal lines and fall at the locus of circles marked 'Vgr.' The offset is largely attributable to differences in the *Voyager* trajectories employed for the two solutions.

Fig. 10 summarizes the pole precession rates on the sky and formal errors for the fits enumerated in Table 4, shown as black circles. For comparison, we show the predicted long term average precession rate on the sky of $\dot{\hat{n}}_P = 0.34''$ yr^{-1} from F93, and their fitted result of 0.86 ± 0.31 times this value (shown in blue). Additional constraints on the pole precession rate can be obtained from precise measurements of Saturn's ring plane crossing times. Bosh et al. (1997) combined the known pole position at the time of the *Voyager* encounters with the observed RPX time on 22 May 1995 to obtain $\Omega_P = 0.52 \pm 0.07''\text{yr}^{-1}$, corresponding to a precession rate on the sky of $\dot{\hat{n}}_P = \Omega_P \sin\epsilon = 0.24 \pm 0.03''\text{yr}^{-1}$, shown in red. From 22 reported RPX times, extending over a period of 280 yr, Nicholson et al. (1999) estimated the angular rate of the pole to be $\Omega_P = 0.51 \pm 0.14''\text{yr}^{-1}$, corresponding to $\dot{\hat{n}}_P = \Omega_P \sin\epsilon = 0.23 \pm 0.06''\text{yr}^{-1}$, shown in green. Nicholson et al. (1999) noted that the low precession rate, compared to the predicted long-term average, results from a slow variation in Titan's torque exerted on Saturn, which at the present time is close to its minimum value, and that the nutation model of Vienne and Duriez (1992) predicts an average precession rate over the 20th century of $\Omega_P = 0.50''\text{yr}^{-1}$ (or $\dot{\hat{n}}_P = 0.23''\text{yr}^{-1}$), 68% of the long-term secular rate. This is in reasonable agreement with both our current occultation results and independent estimates from RPX observations.

As a final comment, our assumption of a linear precession model over the observation intervals of our individual orbit fits could mask short-term nutation in Saturn's pole arising chiefly from Titan, but also from Dione, Rhea, and Tethys, which have nutation amplitudes reaching nearly 0.5° and periods ranging from 2 to 36 years (Vienne and Duriez, 1992). Although a comprehensive model for Saturn's pole precession that includes these nutation terms has not yet been developed, the difference in the mean precession rate and direction between Fit #1 (based on *Cassini* data only) and the longer-term Fit #7 (see Fig. 9 and Table 4) could be evidence of their importance.

6.6. Sensitivity of adopted radius scale to Saturn pole solution

The pole precession rate is reasonably well constrained by these observations, and generally consistent with theoretical expectations, although still not determined with sufficient accuracy to provide new information about Saturn's interior. On the other hand, the pole *direction* at epoch is very accurately known, as shown in Fig. 4. All fits that included corrections for trajectory errors fall in a tight cluster with very little difference in RA and only about 0.1″ difference in declination. The concentric dashed and solid error ellipses correspond respectively to the 3- and 5-σ formal uncertain-

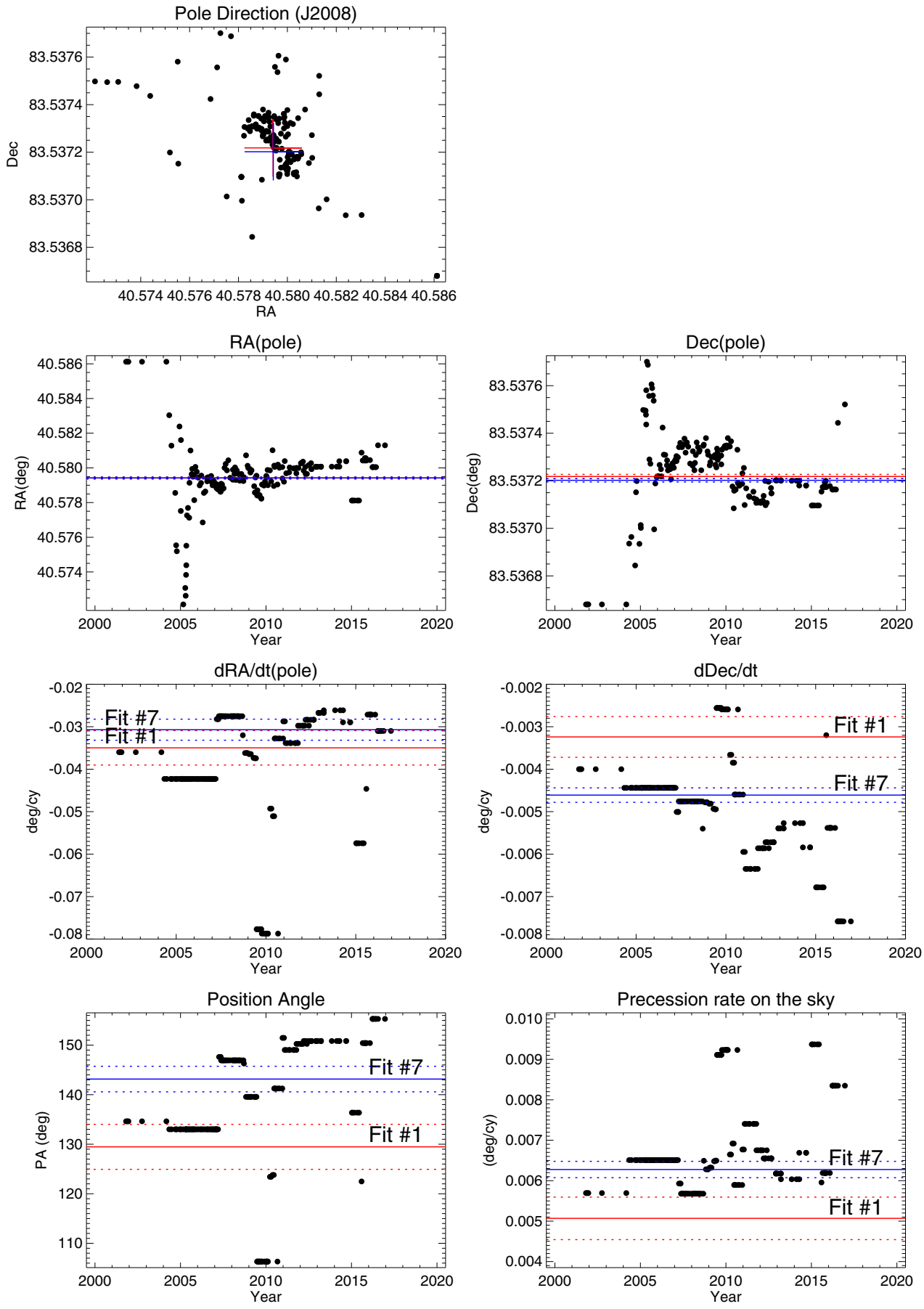

Fig. 12. Variation with time of the assumed Saturn pole direction and precession rate/direction from the *Cassini* Navigation Team's planetary constants files. In each panel, the red symbols/lines correspond to the results from Fit #1 (Table 4) and the blue symbols/lines are from Fit #7. The RA and Dec values of the pole have been precessed from the J2000 epoch in the pck files to the J2008 epoch of our solutions. (For interpretation of the references to colour in this figure legend, the reader is referred to the web version of this article.)

ties of the Fit #7 pole (shown in blue), which we will use to guide our estimates of the sensitivity of the absolute radius scale to the fitted pole solution. We performed four separate fits identical to Fit #7 except in turn holding fixed one of the parameters of the linear pole model, with its value set to $+1-\sigma$ away from the final fitted value from Fit #7; all other parameters were fitted as before. We then compared the fitting ring radii for the 122 features in each fit to the final fitted values from Fit #7.

The results are shown in Fig. 11. Beginning at the upper left, the plot shows the change in radius for each fitted feature resulting from a 1-σ increase in α_P, the RA of the pole at epoch, plotted as a function of orbital radius. The black '+' symbols mark the changes in radius, which are quite small – on the order of a 20 m – for a change in α_P of 0.000044° (see Table 4). As another measure of the sensitivity of the radius scale to changes in the pole direction, we show as red symbols the predicted change in radius based on the correlation between α_P and r_i for the i'th ring. Here, there is a predicted systematic offset of $\simeq -0.005$ km. In the actual fitted case, other parameters that also have correlations with the ring radii are left free to compensate for the increase in the sum of squared residuals resulting from the offset pole direction, accounting for difference between the fit results and simple correlation prediction. For the δ_P case (upper right panel), the correlation and fit results are in better agreement, with typical changes in semimajor axis of about 10 m. The second row of plots shows the relative insensitivity of the radius scale to the precession rate terms, expressed in RA and Dec: changes in radius are at the 10 m level, with isolated exceptions in the A ring that are still below the 50 m level.

If we take the 5-σ error ellipse in Fig. 4 as a conservative estimate of the uncertainty in the fitted pole direction across our set of fits, and scale the results from Fig. 11 by a factor of 5, the resulting *systematic* variations in the radius scale are at most ~ 0.1 km. We regard this as a figure of merit for the internal consistency of our derived radius scale for the variety of data sets and weighting schemes used in our fits, and we now turn to an exploration of possible systematic errors that might affect the *absolute* accuracy of our results.

6.7. Possible systematic errors

Ultimately, the absolute accuracy of the ring radius scale depends on the quality of the fitted data, the validity of the kinematical models to the ring orbits themselves, the geometrical accuracy of end-points of the occultation rays (manifested in the Earth-based station positions, occulted star directions, spacecraft and planetary ephemerides), and the accuracy of the pole precession model, as discussed above. The very small post-fit rms residuals of the fitted rings, shown in Fig. 6, attest to the quality of the data and the applicability of a simple keplerian orbit models (with possible additional normal modes) to the ring features included in the fit. The Earth-based station positions for the 28 Sgr occultation have errors of a few hundred meters or less. For stellar occultations, catalog star positions may be in error by up to $d\theta \sim 0.01''$, but for Earth-based occultations these errors are solved for as part of the overall orbit fit, and for spacecraft stellar occultations, the corresponding *a priori* error in the ring plane intercept radius is only $\sim (0.03/\sin B)$ km for a typical spacecraft range to the ring plane of 10 R_S, where B is the ring opening angle and R_S is Saturn's radius.

We mentioned previously that for spacecraft occultations, *both* ends of the occultation ray have uncertainties, and by far the dominant one is associated with errors in the spacecraft ephemerides. We have adopted a simple approach of solving for along-track timing offsets for the trajectory during each ingress or egress occultation chord, possibly augmented by a slope term in cases where this simple approach leaves uncorrected systematic residuals with ring plane radius (see Eq. (4)). F93 quantified the sensitivity of their pole solution and radius scale to km-scale errors in the *Voyager* trajectories (see F93Table XI), and in the worst case found that ring radii changed by up to 0.284 km. We are using an improved set of *Voyager* ephemerides that are likely to have somewhat smaller errors, but this gives a rough estimate of the dependence of the F93 radius scale on the absolute accuracy of the *Voyager* trajectories.

In our case, the differences in fitted orbital radii between our *Cassini*-only solution (Fit #1, for example) and our final adopted solution are negligible (Fig. 7 and Table 5), so we can focus on the large set of reconstructed *Cassini* ephemerides (Table 2) used in our fits as a potential source of systematic errors still present, even after our first-order trajectory corrections included in our fits. The trajectories for orbits ("revs") near the end of the *Cassini* orbital tour are inherently more accurate than for earlier revs because they build on ephemerides of Saturn and its satellites that have gradually improved with the accumulation of more navigational data over time. It is plausible that residual uncorrected trajectory errors that might affect individual occultation geometric reconstructions are larger in the earlier *Cassini* data than in more recent observations, although this is not reflected in a decrease in the magnitude of the trajectory time offset corrections over the course of time.

One possible source of systematic error is the variation in the assumed Saturn pole model over the course of the *Cassini* orbital tour used in the development of the reconstructed spacecraft ephemerides. Each such kernel has an associated planetary constants file ("pck" file) produced by the *Cassini* Navigation Team that contains a linear precession model for Saturn's pole based on the J2000 epoch, and we have found that there is substantial variation in the pole direction and precession rate/direction in these files, as shown in Fig 12. The top left panel plots the RA and Dec of the pole from the pck files, precessed to the J2008 epoch. In each panel, the red symbols/lines correspond to the fitted pole model from Fit #1 and the blue symbols/lines are from our adopted Fit #7. In subsequent rows, the individual components of the pole model are plotted as a function of the date of the pck file. Notice the large excursions in RA and Dec prior to 2006, and the abrupt change in the Dec of the pole in mid-2010. The pole precession rates and directions show substantial variations over time, expressed in rectangular coordinates (third row) and polar coordinates (bottom row). Each pck file has a restricted time interval of applicability, and as one moves further and further in time from the J2000 epoch, slight changes in the pole precession rate and direction can result in relatively larger changes in the pole direction for the time period appropriate for a given file.

We see from Fig. 12 that no single, self-consistent pole model is incorporated in the pck files associated with all reconstructed trajectory kernels, and that there is considerable scatter even among the most recent values. Without knowing the details of the navigation solution for the reconstructed trajectories, however, it is difficult to assess the significance of these variations. What is clear is that a simple transformation of the reference frame of a given reconstructed trajectory from a Saturn equatorial system based on the pck file pole models to a reference frame based on a self-consistent linear pole precession model would result in unacceptably large errors in the spacecraft position. Nevertheless, spot-checking of a few reconstructed trajectories shows that *some* aspects of the assumed Saturn pole model are present in the reconstructed trajectories (Duane Roth, Cassini Navigation Team, personal communication), which might result in uncorrected systematic errors in the fitted pole direction and radius scale from our fits.

Given the remarkably good agreement between the F93 radius scale based entirely on *Voyager* and 28 Sgr observations, and the

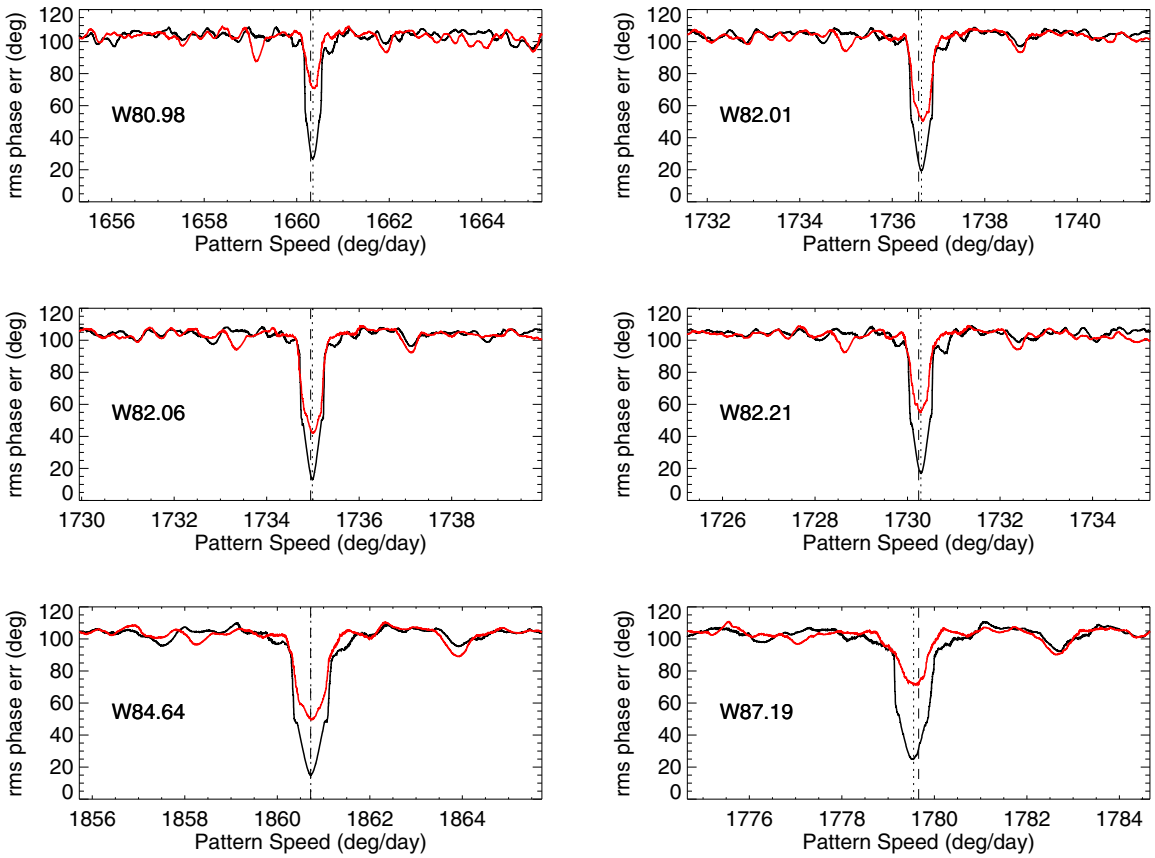

Fig. 13. Comparison of the detectability of six C ring density waves studied by Hedman and Nicholson (2013). Each panel presents a periodogram scan over a range of pattern speeds centered on the theoretical value for the given density wave in question, marked by a vertical dashed line. Each scan shows the rms error in the phase differences between the ensemble of pairs of individual occultation profiles, as discussed in detail by Hedman and Nicholson (2013), and a sharp local minimum (marked by the vertical dotted line) near the predicted pattern speed (dashed vertical line) signals the correct identification of the wavenumber of the density wave in question. The black curves incorporate the trajectory corrections given in Table 1 for Fit #1, and show convincing detections in each case. The red curves show the results based on the nominal occultation geometry of the *Cassini* reconstructed trajectories, without the correction terms from Table 1. The minima are in all cases much shallower, and in the case of W80.98 the detection is marginal at best. (For interpretation of the references to colour in this figure legend, the reader is referred to the web version of this article.)

radius scale from Fit #1 based only on *Cassini* data, it seems unlikely that any systematic errors in the absolute radius scale are larger than a few hundred meters, but this will not be finally resolved until a new set of *Cassini* ephemerides is produced for the entire orbital tour that is based on a self-consistent model for Saturn's pole direction and precession. That will provide an opportunity to revisit the determination of Saturn's pole precession rate and direction as well, which if measured to sufficient accuracy could yield an important constraint on Saturn's moment of inertia and its internal structure. In the meantime, we estimate the overall accuracy of the radius scale to be ± 250 m, based on doubling the 100 m errors estimated from Fig. 11 and allowing for possible uncorrected systematic errors in the *Cassini* trajectories.

6.8. Applications of the new radius scale

Our derived absolute radius scale is in overall excellent agreement with the F93 results, but represents an improvement in several respects. First, we have determined accurate orbits for 122 features across the ring system, greatly expanding the set of fiducial features that can be used to establish an absolute radius scale for spacecraft images with limited radial coverage of the rings. These orbital elements are being used to navigate a comprehensive set of spacecraft images of Saturn's rings that are archived in NASA's Planetary Data System Ring-Moon Systems Node (Robert French, personal communication). Second, our derived trajectory corrections for the 236 individual *Cassini* occultation profiles in Table 1 make it possible to register multiple occultation chords onto a common radius scale to very high relative accuracy – post-fit residuals of individual ring features show that the *relative* alignment of pairs of occultation chords in radius can agree to better than 100 m (even if the *absolute* radius scale is uncertain by 250 m). Such high accuracy makes it possible to compare the detailed phases and shapes of short-wavelength density waves visible in multiple occultations, for example. The efficacy of this approach is shown in Fig. 13. Each panel shows a periodogram scan for the best-fitting pattern speed of a short-wavelength density wave in the C ring, identified by a minimum in the rms phase error between pairs of occultation scans of the density wave at different times and longitudes (see Hedman and Nicholson, 2013 for details). The black curves show the results when the *Cassini* trajectory corrections in Table 1 have been applied to the individual occultations, and in each case there is a clear minimum in the periodogram near the theoretical period appropriate for the wave in question.[5] The red curves show the results of the periodogram scans when the radius scale for each ring profile is computed on the basis of the individual reconstructed trajectories, without including the correction terms obtained from our fits. In all cases, the detection is much less secure, and in the case of the W80.98 wave (located near 80,980 km in the C ring) is marginal at best. A host of previously unidentified waves in the C ring now have the prospect of being decoded with the help of our trajectory corrections.

[5] Note that Hedman and Nicholson (2013) incorporated these *Cassini* trajectory corrections in their analysis.

7. Discussion and conclusions

We have presented a comprehensive solution for the geometry of Saturn's ring system, based on orbital fits to an extensive set of occultation observations of 122 individual ring edges and gaps. We began with a restricted set of very high quality *Cassini* VIMS, UVIS, and RSS measurements for quasi-circular features in the C and B rings and the Cassini Division, and then successively added suitably-weighted additional *Cassini* and historical occultation measurements (from *Voyager, HST* and the widely-observed 28 Sgr occultation of 3 Jul 1989) for additional non-circular features, to derive an absolute radius scale applicable across the entire classical ring system. As part of our adopted solution, we determined first-order corrections to the spacecraft trajectories used to determine the geometry of individual occultation chords.

We used a linear model for Saturn's pole precession, and our favored solution from Fit #7 yields a precession rate on the sky of $\dot{\hat{n}}_P = 0.207 \pm 0.006''\mathrm{yr}^{-1}$, equivalent to an angular rate of polar motion $\Omega_P = 0.451 \pm 0.014''\mathrm{yr}^{-1}$. The formal 3% uncertainty in the fitted precession rate is approaching the point where it can provide a useful constraint on models of Saturn's interior. Our results are largely consistent with independent estimates of the precession rate based on historical RPX times (Nicholson et al., 1999) and from theoretical expectations that account for Titan's 700-yr precession period (Vienne and Duriez, 1992) (see Fig. 10). The fitted precession rate based on *Cassini* data only is somewhat lower, which may be an indication of unmodeled shorter term contributions to Saturn's polar motion from other satellites, or perhaps the result of inconsistencies in the assumed direction of Saturn's pole in the reconstructed *Cassini* spacecraft ephemerides. These will have to be addressed before a more realistic estimate of the precession rate and its uncertainty are obtained.

Overall, the agreement with the widely-used F93 radius scale is excellent, with quite small overall systematic differences ($\lesssim 0.1$ km), but our new solution incorporates many more features across the ring system, and the fitted orbital elements correct for the several-km biases in the radii of many ring features in the F93 catalog that were unresolved because of the large projected diameter of 28 Sgr (see Fig. 8). The formal errors in the fitted radii are generally quite small – on the order of tens of meters (see Table 5 and the detailed results in the SM). Systematic errors stemming from uncertainty in the precession rate of Saturn's pole and its effect on the accuracy of the reconstructed *Cassini* trajectories are somewhat larger, but the absolute radius scale is relatively insensitive even to 5-σ changes in the pole direction or precession rate, and we estimate the combined magnitude of these systematic errors and pole uncertainties to be of order 250 m. This estimate is likely to be improved once a new set of reconstructed *Cassini* trajectories has been developed, based on a self-consistent model for Saturn's pole precession.

We demonstrated the utility of the new radius scale and the associated trajectory corrections in the analysis of short-wavelength density waves in the C ring (see Fig. 13). In online Supplementary Material, we provide in machine-readable form the more than 15,000 individual ring measurements used in this study, along with fitted orbital elements for all 122 ring features and additional details of the orbit fits underlying this work.

8. Appendix

8.1. Sample calculations using Cassini ephemeris corrections

We offer the following examples to assist readers who wish to make use of the *Cassini* trajectory corrections given in Table 1. As a reminder, the corrections apply to the reconstructed trajectory kernels listed in Table 2 and make use of raw occultation data files on NASA's PDS Ring-Moons Node. The second entry (beginning at line 3) in the table is for VIMS_2Cen194I. The first line for this event corresponds to Fit #7, and the second line to Fit #1 (in cases where an event has only one line, it corresponds to the more inclusive Fit #7). The occultation chord itself spans the radial range from 70,000 to 150,000 km (note that the inner edge of the C ring is at 74,490 km and the outer edge of the A ring is at 136,774 km). Within this range, the minimum and maximum radii of features used to establish the trajectory correction for Fit #7 are 74,490 and 136,552 km (i.e., including most of the A ring), and between these two limits the trajectory correction is by interpolation; outside of this range, it is by extrapolation, which is likely to be less accurate if the range of extrapolation is large. The Fit #7 trajectory correction has an along-track time offset $\Delta t = 0.089 \pm 0.004$ s and slope $\alpha = -0.0042 \pm 0.0013$. In all, 76 features were used for this determination, with an unweighted rms of 0.45 km (recall, however, that Fit #7 weights the *Cassini* data ring-by-ring).

The corresponding results for Fit #1 are as follows: the minimum and maximum radii of the 44 fitted features are 74,615 and 120,316 km (notably, this does not extend to the A ring), with a much smaller unweighted rms of 0.14 km. The maximum and minimum differences between the corrected radii from Fit #7 compared to Fit #1 are +0.006 and −0.094 km. The trajectory correction for Fit #1 is $\Delta t = 0.093 \pm 0.006$ s, with no slope term, owing to the shorter radial range covered by the features used in this fit. When trajectory corrections are provided for both Fits #7 and #1, the results for Fit #1 are preferred for features with radii between r'_{min} and r'_{max}, since they are based on a more restricted set of high quality measurements and the trajectory correction is locally optimized within this range. However, for features outside of this interval, Fit #7 is generally preferable. In nearly all cases, the differences between the two solutions will be below 100 m.

As a specific example of the application of the radius scale correction, consider the measured time at the spacecraft of ring ID 9 (Barnard gap OEG) for VIMS_2Cen194I: 2013 JUL 08 15:15:27.5935. The nominal radius (without any trajectory correction) at this time for the pole direction in Fit #1 is 120,316.291 km, and the ring plane radial velocity, obtained by finite differences, is $\dot{r} = -7.48172$ km s^{-1}. From Table 1, $\Delta t = +0.093$ s. The corresponding radial correction is $dr = \dot{r}\Delta t = -7.48172 \times 0.093 = -0.696$ km, and thus the calculated radius including the trajectory correction is 120,315.595 km. By comparison, the nominal radius (without any trajectory correction) at this time from Fit #7 is 120,316.180 km, and $\dot{r} = -7.48171$ km s^{-1}. The corresponding radial correction is $dr = \dot{r}\Delta t - \alpha(r - 100,000)/1000 = -7.48171 \times 0.089 + 0.0042 \times (120,316.180 - 100,000)/1000 = -0.581$ km, and thus the corrected radius is $120,316.180 - 0.581 = 120,315.599$ km.[6] The corrected radii (Fit #7 - Fit #1) differ by only $120,315.599 - 120,315.595 = +0.004$ km in this case.

In cases where a user has a ring occultation profile as a function of radius, but without absolute timing or knowledge of the assumed pole direction or other geometrical factors underlying the calculation of the provided radius scale, conversion to our adopted radius scale is most easily achieved by comparing the measured locations and the fitted values for the radii of the 94 nominally circular features for Fit #7 given in Table 5, and fitting a low-order polynomial correction to the provided radius scale in the vicinity of interest, being mindful of the ring regions where the forced normal modes by Titan and Mimas contribute time-dependent distortions to the radius scale. For users requiring more accurate results, the ring orbital elements for all 122 features included in Fit #7 provided in the SM can be used to compute the radii of non-circular

[6] The online SM file `SM-RINGFIT-Fit7-annotated.txt` gives 120315.5994 for the corrected radius.

features at the time of the occultation in question, at the cost of additional computational effort.

8.2. Online supplementary material

The online Supplementary Material (SM) accompanying this work contains machine readable versions of Tables 1– 5, produced using the American Astronomical Society's machine readable table creator (https://authortools.aas.org/MRT/upload.html), along with both typeset and machine readable tables of ring orbital elements for all 122 features used in this study. These are primarily for users with the computational resources and need for high accuracy who wish to reproduce exactly the geometrical solution underlying this work – for example, to register spacecraft images onto our absolute radius scale. We recommend that users primarily interested in the ring orbital elements themselves as evidence of weak dynamical effects (such as free and forced normal modes) refer instead to Papers 1, 2, and 3, which contain detailed discussions of ring features in question. Upon the conclusion of the *Cassini* orbital mission, we plan to incorporate the full set of ring occultation data into a comprehensive study of all of these features, using improved spacecraft ephemerides and a dynamical model of Saturn's pole precession. That will provide an opportunity to review the dynamical implications of the ring orbits.

The SM also includes observatory locations for the 28 Sgr observations, binary kernel files for the ephemerides for the two *HST* occultations, and individual measurements for the entire set of ring observations used in our orbit fits. We also provide annotated versions of the output files from RINGFIT for Fits #1 and #7 that contain detailed geometrical information about each occultation.

Supplementary material

Supplementary material associated with this article can be found, in the online version, at 10.1016/j.icarus.2017.02.007

Acknowledgments

This work was supported in part by the NASA Cassini project and by NASA Cassini Data Analysis Program Grant NNX09SE66G. The work of R. A. Jacobson was carried out at the Jet Propulsion Laboratory, California Institute of Technology, under a contract with the NASA. We are grateful to two anonymous reviewers for their careful reading of the original manuscript. We would also like to acknowledge the efforts of over two dozen Wellesley College undergraduate students – members of "Team Cassini" – who over the course of several years assisted in the measurements of over 15,000 individual ring occultation observations, making this work possible. The original occultation data were obtained through the efforts of many individuals on the *Cassini* RSS, UVIS, and VIMS science and engineering teams, to whom we express our deep appreciation.

References

Abalakin, V.K., 1981. The IAU system / 1976 1979 / of fundamental astronomical constants. Astronomicheskii Zhurnal 58, 465.
Agency, E.S., 1997. The Hipparcos and Tycho catalogues. ESA SP-1200.
Bosh, A.S., Olkin, C.B., French, R.G., Nicholson, P.D., 2002. Saturn's F ring: Kinematics and particle sizes from stellar occultation studies. Icarus 157, 57–75.
Bosh, A.S., Rivkin, A.S., Percival, J.W., Taylor, M., van Citters, G.W., 1997. Saturn ring-plane crossing, may 1995: pole precession and ring thickness. Icarus 129, 555–561.
Boucher, C., Altamimi, Z., Duhem, L., 1994. Results and analysis of the ITRF93, pp. 1–313. IERS Technical Note 18
Brown, R.H., colleagues, ., 2004. The cassini visual and infrared mapping spectrometer (VIMS) investigation. Space Sci. Rev. 115, 111–168.
Bucciarelli, B., García Yus, J., Casalegno, R., et al., 2001. An all-sky set of (b)-v-r photometric calibrators for schmidt surveys. GSPC2.1: first release. Astron. Astrophys. 368, 335–346.
Colwell, J.E., Esposito, L.W., Sremčević, M., 2006. Self-gravity wakes in saturn's a ring measured by stellar occultations from cassini. Geophys. Res. Lett. 33, L07201.
Colwell, J.E., Nicholson, P.D., Tiscareno, M.S., Murray, C.D., French, R.G., Marouf, E.A., 2009. The structure of saturn's rings. In: Dougherty, M.K., et al. (Eds.), Saturn from Cassini-Huygens. Springer, pp. 375–412.
El Moutamid, M., coauthors, ., 2016. How Janus' orbital swap affects the edge of Saturn's A ring. Icarus 279, 125–140.
Elliot, J.L., Bosh, A.S., Cooke, M.L., Bless, R.C., Nelson, M.J., Percival, J.W., Taylor, M.J., Dolan, J.F., Robinson, E.L., van Citters, G.W., 1993. An occultation by saturn's rings on 1991 october 2–3 observed with the hubble space telescope. Astron. J. 106, 2544–2572.
Esposito, L.W., colleagues, ., 2004. The cassini ultraviolet imaging spectrograph investigation. Space Sci. Rev. 115, 299–361.
Esposito, L.W., Harris, C.C., Simmons, K.E., 1987. Features in saturn's rings. Astrophys. J. Suppl. Ser. 63, 749–770.
Esposito, L.W., Ocallaghan, M., West, R.A., 1983. The structure of saturn's rings – implications from the voyager stellar occultation. Icarus 56, 439–452.
French, R.G., colleagues, ., 1993. Geometry of the saturn system from the 3 july 1989 occultation of 28 sgr and voyager observations. Icarus 103, 163–214.
French, R.G., Marouf, E.A., Rappaport, N.J., McGhee, C.A., 2010. Occultation observations of saturn's b ring and cassini division. Astron. J. 139, 1649–1667.
French, R.G., Nicholson, P.D., Hedman, M.M., Hahn, J.M., McGhee-French, C.A., Colwell, J.E., Marouf, E.A., Rappaport, N.J., 2016a. Deciphering the embedded wave in saturn's maxwell ringlet. Icarus 279, 62–77.
French, R.G., Nicholson, P.D., McGhee-French, C.A., Lonergan, K., Sepersky, T., Hedman, M.M., Marouf, E.A., Colwell, J.E., 2016. Noncircular features in saturn's rings III: the cassini division. Icarus 274, 131–162.
Giorgini, J.D., Yeomans, D.K., Chamberlin, A.B., Chodas, P.W., Jacobson, R.A., Keesey, M.S., Lieske, J.H., Ostro, S.J., Standish, E.M., Wimberly, R.N., 1996. JPL's on-line solar system data service. Bull. Am. Astron. Soc. 28, 25.04.
Hedman, M.M., Nicholson, P.D., 2013. Kronoseismology: using density waves in Saturn's C ring to probe the planet's interior. Astron. J. 146, 12.
Hedman, M.M., Nicholson, P.D., 2014. More kronoseismology with Saturn's rings. Mon Not R Astron Soc 444, 1369–1388.
Hedman, M.M., Nicholson, P.D., Baines, K.H., Buratti, B.J., Sotin, C., Clark, R.N., Brown, R.H., French, R.G., Marouf, E.A., 2010. The architecture of the cassini division. Astron. J. 139, 228–251.
Holberg, J.B., Forrester, W.T., Lissauer, J.J., 1982. Identification of resonance features within the rings of saturn. Nature 297, 115–120.
Hubbard, W.B., colleagues, ., 1993. The occultation of 28 SGR by saturn – saturn pole position and astrometry. Icarus 103, 215–234.
Kliore, A.J., colleagues, ., 2004. Cassini radio science. Sp. Sci. Rev. 115, 1–70.
Lane, A.L., Hord, C.W., West, R.A., Esposito, L.W., Coffeen, D.L., Sato, M., Simmons, K.E., Pomphrey, R.B., Morris, R.B., 1982. Photopolarimetry from voyager 2 – preliminary results on saturn, titan, and the rings. Science 215, 537–543.
Marouf, E.A., Tyler, G.L., Rosen, P.A., 1986. Profiling Saturn's rings by radio occultation. Icarus 68, 120–166.
Nicholson, P.D., Cooke, M.L., Pelton, E., 1990. An absolute radius scale for Saturn's rings. Astron. J. 100, 1339–1362.
Nicholson, P.D., French, R.G., Bosh, A.S., 1999. Ring plane crossings and Saturn's pole precession. AAS/Division for Planetary Sciences Meeting Abstracts #31 31, 44.01.
Nicholson, P.D., French, R.G., Hedman, M.M., Marouf, E.A., Colwell, J.E., 2014a. Noncircular features in saturn's rings I: the edge of the B ring. Icarus 227, 152–175.
Nicholson, P.D., French, R.G., McGhee-French, C.A., Hedman, M.M., Marouf, E.A., Colwell, J.E., Lonergan, K., Sepersky, T., 2014. Noncircular features in Saturn's rings II: the C ring. Icarus 241, 373–396.
Sandel, B.R., colleagues, ., 1982. Extreme ultraviolet observations from the voyager 2 encounter with saturn. Science 215, 548–553.
Simpson, R.A., Tyler, G.L., Holberg, J.B., 1983. Saturn'S pole - geometric correction based on voyager UVS and radio occultations. Astron. J. 88, 1531–1536.
Skrutskie, M.F., colleagues, ., 2006. The two micron all sky survey (2MASS). Astron. J. 131, 1163–1183.
Smith, B.A., colleagues, ., 1981. Encounter with saturn - voyager 1 imaging science results. Science 212, 163–191.
Smith, B.A., colleagues, ., 1982. A new look at the saturn system - the voyager 2 images. Science 215, 504–537.
Tajeddine, R., Nicholson, P.D., Tiscareno, M.S., Hedman, M.M., Burns, J.A., 2017. Dynamical phenomena at the inner edge of the keeler gap. Icarus. (submitted)
Tyler, G.L., Marouf, E.A., Simpson, R.A., Zebker, H.A., Eshleman, V.R., 1983. The microwave opacity of saturn's rings at wavelengths of 3.6 and 13 cm from voyager 1 radio occultation. Icarus 54, 160–188.
Vienne, A., Duriez, L., 1992. A general theory of motion for the eight major satellites of saturn. III - long-period perturbations. Astron. Astrophys. 257, 331–352.
Vienne, A., Duriez, L., 1995. TASS1.6: Ephemerides of the major saturnian satellites. Astron. Astrophys. 297, 588.
Ward, W.R., 1975. Tidal friction and generalized cassini's laws in the solar system. Astron. J. 80, 64–70.